Icarus 354 (2021) 114094

Contents lists available at ScienceDirect

Icarus

journal homepage: www.elsevier.com/locate/icarus

Research Paper

Asteroid phase curves from ATLAS dual-band photometry☆

Max Mahlke [a,b,*], Benoit Carry [a], Larry Denneau [c]

[a] Université Côte d'Azur, Observatoire de la Côte d'Azur, CNRS, Laboratoire Lagrange, France
[b] CAB (INTA-CSIC), Campus ESAC (ESA), Villanueva de la Cañada, Madrid, Spain
[c] University of Hawaii, 2680 Woodlawn Dr., Honolulu, HI 96822, USA

ARTICLE INFO

Keywords:
Asteroids
Composition
Surfaces
Photometry

ABSTRACT

Asteroid phase curves are used to derive fundamental physical properties through the determination of the absolute magnitude H. The upcoming visible *Legacy Survey of Space and Time* (LSST) and mid-infrared *Near-Earth Object Surveillance Mission* (NEOSM) surveys rely on these absolute magnitudes to derive the colours and albedos of millions of asteroids. Furthermore, the shape of the phase curves reflects their surface compositions, allowing for conclusions on their taxonomy. We derive asteroid phase curves from dual-band photometry acquired by the *Asteroid Terrestrial-impact Last Alert System* telescopes. Using Bayesian parameter inference, we retrieve the absolute magnitudes and slope parameters of 127,012 phase curves of 94,777 asteroids in the photometric H, G_1, G_2- and H, G_{12}*-systems. The taxonomic complexes of asteroids separate in the observed G_1, G_2-distributions, correlating with their mean visual albedo. This allows for differentiating the X-complex into the P-, M-, and E-complexes using the slope parameters as alternative to albedo measurements. Further, taxonomic misclassifications from spectrophotometric datasets as well as interlopers in dynamical families of asteroids reveal themselves in G_1, G_2-space. The H, G_{12}*-model applied to the serendipitous observations is unable to resolve target taxonomy. The G_1, G_2 phase coefficients show wavelength-dependency for the majority of taxonomic complexes. Their values allow for estimating the degree of phase reddening of the spectral slope. The uncertainty of the phase coefficients and the derived absolute magnitude is dominated by the observational coverage of the opposition effect rather than the magnitude dispersion induced by the asteroids' irregular shapes and orientations. Serendipitous asteroid observations allow for reliable phase curve determination for a large number of asteroids. To ensure that the acquired absolute magnitudes are suited for colour computations, it is imperative that future surveys densely cover the opposition effects of the phase curves, minimizing the uncertainty on H. The phase curve slope parameters offer an accessible dimension for taxonomic classification, correlating with the albedo and complimentary to the spectral dimension.

1. Introduction

The absolute magnitude H of asteroids is defined as their apparent Johnson V-band magnitude observed at zero degree solar phase angle and reduced to 1 AU distance from both the Sun and the Earth, averaged over a full period of their rotation. The phase angle α is the angle between the Sun, the asteroid, and the observer. The reduced magnitude $V(\alpha)$ is calculated from the observed apparent magnitude m as

$$V(\alpha) = m + 5log(r\Delta) \quad (1)$$

where r is the distance between the asteroid and the Sun at the epoch of observation and Δ the respective distance between the asteroid and Earth. $V(\alpha)$ is referred to as the phase curve, and, by definition, $H = V(0)$.

The inference of principal physical parameters of minor bodies requires accurate knowledge of their absolute magnitudes. Their diameter D and visual geometric albedo p_V are related to H by (Harris and Lagerros, 2002)

$$log_{10}D = 3.1236 - 0.2H - 0.5log_{10}p_V \quad (2)$$

Any uncertainty in H enters logarithmically in the derivation of the physical properties. The diameters and visual albedos of more than 100,000 Main Belt asteroids observed with NASA's *Wide-field Infrared*

☆ The catalogue of absolute magnitudes and phase parameters is publicly available at the CDS via anonymous ftp to cdsarc.u-strasbg.fr (130.79.128.5) or via http://cdsarc.u-strasbg.fr/viz-bin/qcat?VII/288.

* Corresponding author at: Université Côte d'Azur, Observatoire de la Côte d'Azur, CNRS, Laboratoire Lagrange, France.
E-mail address: max.mahlke@oca.eu (M. Mahlke).

https://doi.org/10.1016/j.icarus.2020.114094
Received 4 June 2020; Received in revised form 17 August 2020; Accepted 31 August 2020
Available online 14 September 2020

Survey Explorer (WISE) carry 20% and 40% accuracy, under the assumption that the referenced absolute magnitudes are accurate (Masiero et al., 2011; Nugent et al., 2015). NASA's planned *Near-Earth Object Surveillance Mission* (NEOSM, previously NEOCam, Grav et al., 2019) aims to extend this catalogue by an order of magnitude, thereby vastly increasing the demand for accurate determinations of H.

Deriving H in different wavelength bands further offers the consolidation of asteroid photometry obtained at different epochs for colour computation and subsequent taxonomic classification. This is vital for the upcoming *Legacy Survey of Space and Time* (LSST) executed at the Vera C. Rubin Observatory. The LSST aims to provide catalogues of photometric variability and colours for millions of minor bodies (Jones et al., 2009). The latter necessitates either quasi-simultaneous multi-band observations of a single target or reduction of the observed magnitudes to zero phase angle (Szabó et al., 2004; Warner et al., 2009). Given the numerous competing science cases of the LSST and its planned operations with two filters per night at most, the Solar System science community cannot rely on the realization of the required observation cadence alone. Instead, H must be derived in each band by fitting the observed phase curves to obtain the colours.

The definition of H requires asteroid magnitudes at zero degree phase angle. This is practically difficult to achieve, hence H is instead extrapolated from photometric observations acquired close to opposition, but at non-zero phase angles, by means of phase curve modelling. We summarize here the most basic modelling advances and refer to Muinonen et al. (2002) and Li et al. (2015) for detailed reviews.

In first order, an asteroid's apparent brightness increases linearly with decreasing phase angle. The slope of the phase curve is dictated by mutual shadowing of the surface particles, which in turn depends on the surface properties like shape, roughness and porosity. When observing an asteroid close to opposition, a nonlinear brightness surge occurs, referred to as *opposition effect* (Gehrels, 1956). In 1985, the *International Astronomical Union* (IAU) adopted the H, G-magnitude system, where G describes the overall slope of the phase curve (Bowell et al., 1989). The H, G-system successfully describes phase curves in large ranges of the phase space, however, it fails to reproduce the opposition effect, especially for exceptionally dark or bright objects (Belskaya and Shevchenko, 2000). In 2010, the H, G system was extended by Muinonen et al. (2010) to the three-parameter H, G_1, G_2-system,

$$V(\alpha) = H - 2.5log_{10}[G_1\Phi_1(\alpha) + G_2\Phi_2(\alpha) + (1 - G_1 - G_2)\Phi_3(\alpha)] \quad (3)$$

where the Φ_i are basis functions describing the linear part (subscripts 1 and 2) and the opposition effect (subscript 3). For low-accuracy and sparsely-sampled phase curves, the authors propose the H, G_{12}-system, later refined by Penttilä et al. (2016) to the H, G_{12}*-system, where

$$(G_1, G_2) = \begin{pmatrix} 0 \\ 0.53513350 \end{pmatrix} + G_{12}^{*} \begin{pmatrix} 0.84293649 \\ -0.53513350 \end{pmatrix} \quad (4)$$

Taking into account the physical constraint that asteroids get fainter with increasing phase angle, we confine the G_1, G_2-space using equ: hg1g2 to

$$G_1, G_2 \geq 0 \quad (5a)$$

$$1 - G_1 - G_2 \geq 0 \quad (5b)$$

We gain physical interpretability of the phase coefficients by expressing the photometric slope k between 0 deg. and 7.5 deg. following Muinonen et al. (2010) as

$$k = -\frac{1}{5\pi}\frac{30G_1 + 9G_2}{G_1 + G_2} \quad (6)$$

and the size of the opposition effect $\zeta - 1$ as

$$\zeta - 1 = \frac{1 - G_1 - G_2}{G_1 + G_2} \quad (7)$$

where ζ is the ratio of the amplitude of the opposition effect and the background intensity. k is in units of mag/rad, while $\zeta - 1$ gives the contribution of the opposition effect to the absolute magnitude in units of mag. Belskaya and Shevchenko (2000) showed that the opposition effect and the photometric slope correlate with the albedo. The former peaks for moderate-albedo asteroids, while minor bodies with high- and low-albedo asteroids display smaller opposition effects. k is proportional to the albedo, with dark asteroids exhibiting steeper phase curves than bright minor bodies.

The derivation of accurate phase curve parameters requires multiple observational campaigns at different solar elongations of a single target. The observations need to account for the modulation of the apparent magnitude by the asteroid's irregular shape and rotation, in addition to possible offsets due to varying aspect angles when combining data from distinct apparitions. Examples of targeted campaigns can be found in Shevchenko et al. (1997, 2002, 2008, 2016). The number of asteroids with accurate and reduced phase curves available remains in the lower hundreds due to the requirements of extensive telescope time and asteroid shape models.

To obtain catalogues of phase curve parameters in the order of magnitude required for future large-scale surveys, serendipitous asteroid observations need to be exploited. Oszkiewicz et al. (2011) determined the H, G_1, G_2- and H, G_{12}-model values of more than 500,000 asteroids by combining observations from different observatories.[1] Since the publication of this catalogue, the number of known minor planets has increased almost two-fold. We aim to extend this effort while taking note of two caveats of the analysis. First, the fitted H, G_1, G_2- and H, G_{12}-model were not constrained as in Eq. 5b, resulting in 52% of the reported slope parameters lying outside the physical range. Furthermore, the authors combined observations from different wavebands, applying average asteroid colour-indices to unify the data. However, the slopes and band widths of asteroid spectra increase with increasing phase angle (e.g., Shkuratov et al., 2002; Sanchez et al., 2012), resulting in wavelength-dependent phase curves. Therefore, we refrain from combining observations acquired in different wavebands.

Utilising serendipitous observations offers the advantage of large catalogues, however, the derived phase curves are subject to several undesirable effects. The majority of observations reported to the *Minor Planet Centre* (MPC)[2] is collected by large-scale surveys aiming to monitor the near-Earth environment. To identify asteroids on collision trajectories with Earth, these surveys favour observing asteroids in quadrature rather than opposition. This introduces a bias towards observations at the maximum observable phase angle for asteroid populations with superior orbits to that of Earth. In addition, the light curve modulation introduced by rotation and apparition effects can be reduced using accurate targeted observations, e.g. by means of a Fourier analysis to derive the shape of the light curve and by treating observations from multiple oppositions separately. For non-targeted observations, the comparatively large photometric uncertainty inhibits such a reduction. Furthermore, the corresponding increase in required observations would decrease the size of the available sample, diminishing the statistical significance of the resulting catalogue. As a consequence, serendipitously observed phase curves exhibit stochastic fluctuations, translating into larger uncertainties on the fitted phase coefficients.

In this work, we derive the phase curve parameters of serendipitously observed asteroids. In Section 2, we describe the observations at hand and the Bayesian parameter inference approach. The fitted phase curve parameters are summarized in Section 3. The taxonomic interpretability of the G_1, G_2-parameters and their wavelength-dependency are outlined in Section 4. We illustrate these results with the

[1] https://wiki.helsinki.fi/display/PSR/Asteroid+absolute+magnitude+and+slope.

[2] https://minorplanetcenter.net.

taxonomy of asteroid families in Section 5. In Section 6, we quantify the effect of various sources of uncertainties and limited phase curve coverage at opposition on the derived phase curve parameters. The conclusions are presented in Section 7.

2. Methodology

2.1. Selection of serendipitous observations

The MPC observations database contains 246 million asteroid observations as of March 2020. We aim to acquire densely sampled phase curves for a large, unbiased corpus of asteroids. At the same time, we seek to quantify the inherent effects of the asteroids' shape-induced light curve modulation on the phase curve parameters. We therefore attempt to exclude possible sources of systematic effects rigorously. These derive foremost from non-homogeneous photometry between different observatories. Differences in the filter transmission, reduction pipeline, or stellar catalogues introduce discrepancies in the reported magnitudes of asteroids.

Instead, we choose to utilise observations from a single observatory, maximising the likelihood of consistent data treatment. In recent years, both the *Panoramic Survey Telescope and Rapid Response System* (Pan-STARRS, Hodapp et al. (2004)) and the *Asteroid Terrestrial-impact Last Alert System* (ATLAS, Tonry et al. (2018)) have placed among the top five contributors to the MPC in terms of number of observations. Comparing the ephemerides at the epoch of observation of several thousand asteroids observed by the surveys, we find that the bias towards observation at asteroid quadrature is less pronounced in the ATLAS catalogues. In addition, ATLAS has acquired dual-band photometry of a large number of asteroids at comparable phase angles, offering an excellent dataset to investigate the wavelength-dependency of the phase curves. Hence, we make use of observations by ATLAS, referring the reader to Vereš et al. (2015) for a derivation of H, G-parameters using Pan-STARRS observations.

2.2. ATLAS

ATLAS is a NASA-funded sky-survey aiming to observe *near-Earth asteroids* (NEAs) on impactor trajectories with the Earth. It was designed with a focus on a high survey speed per unit cost (Tonry, 2011). Two independent 0.5 m telescopes located at Haleakala and Mauna Loa in Hawaii are in operation since 2015 and 2017 respectively, achieving multiple scans of the northern sky every night. Each telescope observes a 30 deg.^{2} field-of-view. By March 2020, ATLAS has discovered 426 NEAs, including 44 potentially hazardous ones.[3] Standard observations are carried out in two filters, a bandpass between 420 and 650 nm termed *cyan* and a bandpass between 560 and 820 nm termed *orange*. The transmission curves of these filters are depicted in Fig. 1. The observed asteroid astrometry and photometry are reported to the MPC.

We received dual-band photometry of 180,025 distinct asteroids from the ATLAS collaboration. A third of the objects was observed at phase angles below 1 deg. The observations were acquired between June 2015 and December 2018. We extend this database by including ATLAS observations from 2019 reported to the MPC.

The original database contained 26.8 million observations, to which we add 8 million using the MPC database. The required ephemerides are retrieved using the IMCCE's Miriade tool[4] (Berthier et al., 2008). All 180,025 asteroids were observed in *orange*, while 179,719 were observed in *cyan* as well. A small fraction of visually inspected phase curves showed large outlier magnitudes likely caused by blended sources in the images. We remove these detections by rejecting observations where the difference between the predicted and the observed apparent magnitude was larger than 1 mag. This cut is well above the amplitude modulation of asteroid light curves induced by the spin (Marciniak et al., 2015; Carry, 2018).

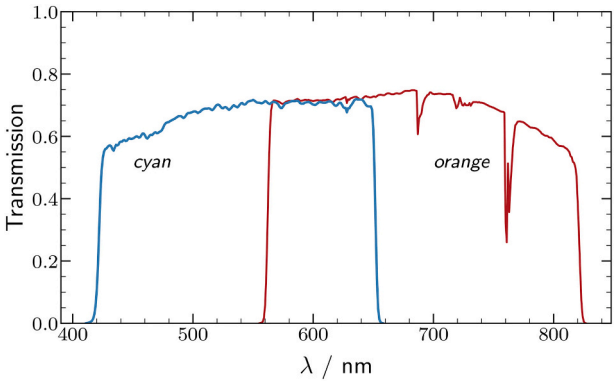

Fig. 1. Transmission curves of the *cyan* and *orange* filters used by the ATLAS survey (Tonry et al., 2018). Data from the Filter Profile Service of the Spanish Virtual Observatory (Rodrigo et al., 2012). http://svo2.cab.inta-csic.es/svo/theory/fps3/. (For interpretation of the references to colour in this figure legend, the reader is referred to the web version of this article.)

2.3. Phase parameter inference

Fitting scattering model functions to phase curves is notoriously ambiguous and the results do not necessarily describe the observed surface, especially in the case of observations where the shape-induced light curve modulation has not been subtracted (Karttunen and Bowell, 1989; Kaasalainen et al., 2003). We choose a computationally expensive Bayesian parameter inference with *Markov chain Monte Carlo* (MCMC) simulations to fit the H, G_1, G_2- and H, G_{12}*-models, allowing to examine the posterior distributions of the phase curve parameters. To differentiate between the absolute magnitudes obtained with these two models, we use the subscript H_{12} for H, G_{12}*.

For both absolute magnitudes H and H_{12}, we choose a weakly informative, normally distributed prior,

$$p(H), p(H_{12}) = \mathcal{N}(\mu = 10, \sigma = 100), \tag{8}$$

where $\mathcal{N}(\mu, \sigma)$ describes the Gaussian normal distribution with mean μ and standard deviation σ. The mean and standard deviation are set to approximate a uniform distribution over the relevant absolute magnitude parameter space. Alternatively, informative prior distributions could be derived from the distribution of the absolute magnitude of Main-Belt asteroids, up to the limiting magnitude of ATLAS (m $\sim$ 19, Tonry et al., 2018), or from computing least-squares fits of the HG-model to each phase curve and using the acquired H and its uncertainty as moments of the Gaussian distribution.

To quantify the effect of the prior choice, we computed the H, G_1, G_2- and H, G_{12}*-model fits for 100 randomly chosen phase curves using the three outlined priors. The distribution of H for Main-Belt objects is approximated with a Gaussian distribution with $\mu = 17.2$ and $\sigma = 1.6$. The resulting distributions of the model parameters H and H_{12} show negligible variation with averaged differences below 0.01, only the prior based on the HG-model yields larger H-values with an averaged difference of 0.06 as it limits the size of the opposition effect. The quantification supports the choice of the weakly informative choice, though the prior based on the Main-Belt magnitudes would have been equally

[3] http://atlas.fallingstar.com.
[4] http://vo.imcce.fr/webservices/miriade/.

acceptable.

Following the slope parameter constraints in Eq. 5, we choose uniform distributions between 0 and 1 as prior probabilities for G_1, G_2, and G_{12}*,

$$p(G_1), p(G_2), p(G_{12}^*) = \mathscr{U}[0,1] \tag{9}$$

Note that this choice in priors does not necessarily lead to G_1 and G_2 satisfying constraint 5b. To accommodate for this, we remove solutions where $1 - G_1 - G_2 < 0$ from the MCMC samples.

In the following, we collectively describe the parameters of the respective photometric model using Θ.

We define the likelihood function by assuming that the observed apparent magnitudes m_α at phase angle α_i follow a normal distribution with the true apparent magnitude as mean and a standard distribution $\sigma_{\alpha,\,i}$ dictated by the asteroid's light curve modulation and the observation accuracy,

$$p(m_\alpha|\Theta) = \mathscr{N}(\mu = \mathbf{m}_{\alpha,i}, \sigma = \sigma_{\alpha,i}) \tag{10}$$

With the given prior probabilities, likelihood function and data, the posterior probability distribution $p(\Theta|m)$ is defined. However, we cannot derive it analytically and need to approximate it by means of MCMC simulations.

We use the pymc3 python package (Salvatier et al., 2016)[5] to perform these simulations. The photometric models are implemented in the sbpy package (Mommert et al., 2019).[6] As best-fit parameters, we use the mean values of the respective parameter's posterior probability distribution. The uncertainties are given by the bounds of the 95% *highest density interval* (HDI) of the posterior distributions.

In Fig. 2, we depict the parameter inference for the phase curve of (20) *Massalia*, as observed by Gehrels (1956), who first noted the opposition effect on the surface of an asteroid using these targeted observations. The resulting H, G_1, G_2- and H, G_{12}*-model fits are displayed, including the 1 D- and 2 D distributions of the G_1 and G_2 MCMC samples. The joint distribution of G_1, G_2 illustrates that the uncertainty in the fit derives primarily from the photometric slope k as opposed to the size of the opposition effect, as can be seen in the uncertainty profile of the fitted phase curve (dashed lines). Nevertheless, the posterior distributions of G_1 and G_2 are Gaussians with comparatively small standard deviations due to the targeted nature of the observations.

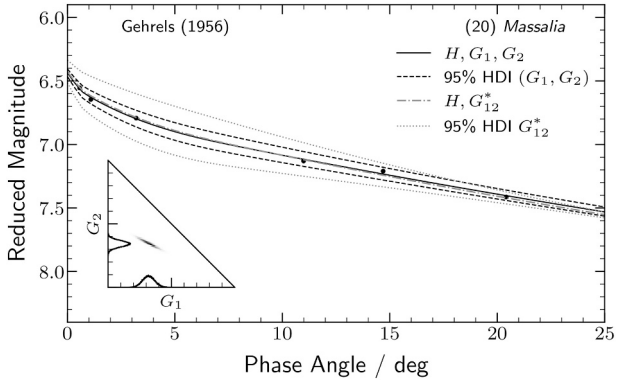

Fig. 2. The phase curve of (20) *Massalia*, as observed by Gehrels (1956), fitted with the H, G_1, G_2-model (solid black). The black dashed curves are plotted using the 95% highest density interval (HDI) values of the three fit parameters. The gray, dash-dotted line represents the H, G_{12}*-model fit with the gray dotted line representing the uncertainty envelope. The measurement uncertainties of 0.01 mag are smaller than the marker size. The inset shows the 1 D- and 2 D-distributions of the G_1 and G_2 Markov chain Monte Carlo samples.

In comparison, we show the effect of serendipitous observations on the parameter inference in Fig. 3, which depicts the H, G_1, G_2- and H, G_{12}*-model fits to observations of (442) *Eichsfeldia* by ATLAS in *cyan*. The same range of reduced magnitudes is given on the y-axis as in Fig. 2. The light curve modulation yields a large dispersion in reduced magnitude at each phase angle, which is reflected in the dispersion of MCMC G_1, G_2-samples, depicted in the plot inset. We further observe that the posterior distribution tends towards the unphysical $G_2 < 0$-regime, likely due to the step in reduced magnitude around 27 deg. phase angle.

Fig. 3 shows that the two photometric models arrive at similar slopes, while the size of the opposition effect and the inferred absolute magnitudes vary considerably ($H = 9.87$, $H_{12} = 9.98$). This highlights the restricted nature of the H, G_{12}*-model; the G_1, G_2-parameters of (442) *Eichsfeldia* in *cyan* are (0.64, 0.05), which is distant from the linear G_1, G_2-relation of G_{12}*. Hence, the H, G_{12}*-model cannot adequately describe the opposition effect of the phase curve.

3. Results

In this section, we present the phase curve parameters acquired by applying the H, G_1, G_2- and H, G_{12}*-models to the serendipitous ATLAS observations. Erasmus et al. (2020) investigate the taxonomic interpretability of the *cyan* - *orange* colour to identify asteroid family members. We highlight the differences in the absolute magnitudes derived with the H, G_1, G_2- and H, G_{12}*-model.

3.1. Sample selection and data availability

From the 180,025 asteroids observed by ATLAS, we select the ones with at least one observation at a phase angle α below three degree, $\alpha_{\min} \leq 3$ deg., to ensure an adequate description of the opposition effect. This decreases the sample size to 124,072 asteroids, rejecting almost a third of the available sample. We choose this limit based on the significant importance of the opposition effect on the phase curve parameters, and after simulating different degrees of incomplete phase curve coverage towards opposition, refer to Section 6. We further apply lower limits on the number of observations, $N \geq 50$, and the maximum phase angle of

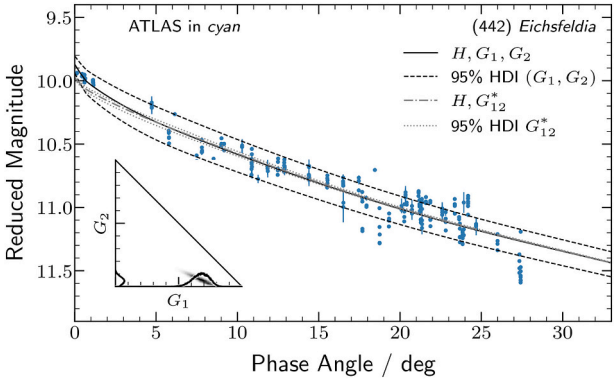

Fig. 3. Like fig:massalia_phase_fit, using the non-targeted ATLAS observations of (442) *Eichsfeldia* in *cyan* instead. The H, G_{12}*-model deviates towards the opposition effect as the G_1, G_2-parameters of the asteroid are outside the definition of G_{12}*. This further leads to the unreasonably small 95% highest density interval of the G_{12}* parameter. (For interpretation of the references to colour in this figure legend, the reader is referred to the web version of this article.)

[5] https://docs.pymc.io/.
[6] https://sbpy.readthedocs.io/.

observation, $\alpha_{\max} \geq 10$ deg., to remove sparsely-sampled phase curves. The final sample consists of 94,777 unique asteroids, 36,441 observed in *cyan* and 90,571 observed in *orange*.

We provide the H, G_1, G_2- and H, G_{12}*-model parameters for all 127,012 fitted phase curves in an online catalogue publicly available at the *Centre de Données astronomiques de Strasbourg* (CDS).[7] The format of the catalogue is described in Appendix A. For 43 phase curves, the H, G_1, G_2-model failed to fit the phase curve, meaning that not a single of the 48,000 MCMC samples satisfied Eq. 5. By visually inspection, we found that large magnitude dispersions, insufficient sampling, or strong apparitions effects lead to unphysical shapes of the phase curves, where the magnitude decreased with increasing phase angle. An example is given in Fig. 10 in Section 6 for the phase curve of (250) *Bettina*, exhibiting a particularly strong apparition effect.

3.2. Phase curve parameters in cyan and orange

We display the absolute magnitudes H and H_{12} in *cyan* and *orange* derived from the model fits on the left hand side of Fig. 4. It is apparent that the absolute magnitudes from the H, G_{12}*-model are lower on average. This is highlighted in the right hand side part of Fig. 4, where we display the histograms of the difference $H - H_{12}$ for all objects. Both in *cyan* and in *orange*, the distributions peak around 0.1 mag and extend up to 1 mag absolute difference.

The origin of these discrepancies can be seen in Fig. 5. On the left hand side, we give the 2 D *kernel density estimator* (KDE) distribution fitted to the G_1, G_2-pairs of the whole sample in *cyan* and *orange* using a

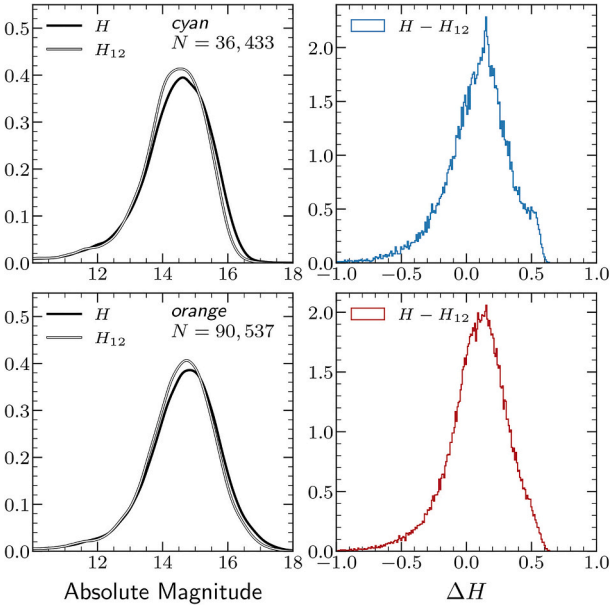

Fig. 4. *Left:* The distribution of absolute magnitudes H (black) and H_{12} (white) derived from ATLAS phase curves of 94,777 asteroids using the H, G_1, G_2- and H, G_{12}*-models respectively, for phase curves observed in *cyan* (top) and *orange* (bottom). For readability, magnitudes below 10 (0.8% of the sample) are not shown. *Right:* The difference in the absolute magnitude derived with the two models, for phase curves in *cyan* (top) and *orange* (bottom). (For interpretation of the references to colour in this figure legend, the reader is referred to the web version of this article.)

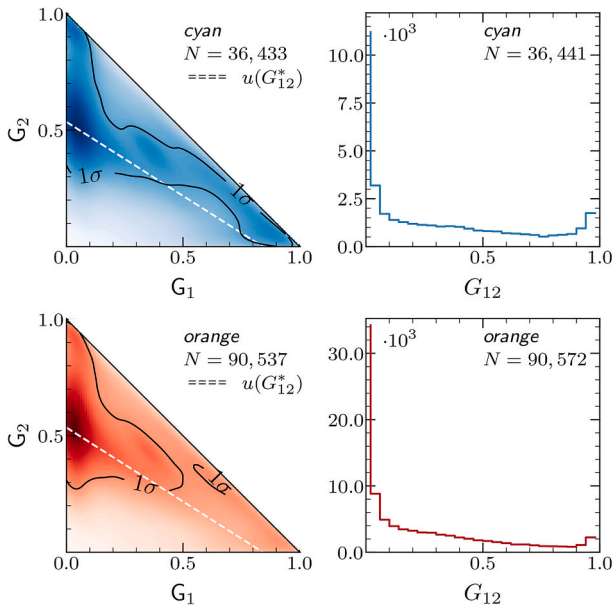

Fig. 5. *Left:* The 2 D-KDE distribution fitted to the G_1, G_2 parameters of the phase curves observed in *cyan* (top) and *orange* (bottom). The black contours outline the 1 σ-levels of the KDE distributions. *Right:* The histogram of the G_{12}*-parameter derived from the same sample of phase curves, aligned in the same order. (For interpretation of the references to colour in this figure legend, the reader is referred to the web version of this article.)

Gaussian kernel. The black 1 σ-contour gives the KDE level at which 68% of the summed probabilities is contained in the area, resembling the 1 σ-level of a Gaussian distribution. The G_{12}*-parameter space is superimposed as white, dashed line (refer to Eq. 4). We observe a clustering towards low G_1, medium G_2 values in both wavebands, centered around the region where we expect S-type asteroids to be located (refer to Section 4). S-types dominate the inner and middle Main Belt in terms of absolute number (DeMeo and Carry, 2013). The distributions further extend towards larger photometric slopes to the region of low-albedo complexes such as the C-types, with a larger fraction of low-albedo asteroids visible in the *cyan* -band. Further noticeable is an extension of distributions towards $G_2 = 1$, i.e. negligible photometric slopes and opposition effects, indicative of high-albedo complexes.

In both wavebands, the majority of asteroids exhibits G_1, G_2-values above the G_{12}*-definition in G_1, G_2-space. The H, G_{12}*-model therefore fails at describing these phase curves, particularly the size of the opposition effect will be overestimated for objects above the G_{12}*-line. $\zeta - 1$ increases non-linearly towards the origin of G_1, G_2-space, leading to the large tail towards negative differences of the distributions on the right hand side of Fig. 4.

The G_{12}*-parameters of the phase curves are depicted in the histograms on the right hand side of Fig. 5. 42% of the sample in *cyan* and 50% of the sample in *orange* are below 0.1, resembling closely the distribution in G_1, G_2-space. In both bands, we observe a decline of the number of objects towards larger G_{12}* values up to about 0.9, where the number rises again. These tendencies of G_{12}* towards the limiting 0 and 1 values indicate that a large number of phase curve lies outside the defining relation, hence, they cannot be represented appropriately by the model. We point out that we observe phase curves fitted with H, G_1, G_2 on the edges of G_1, G_2-space as well, though in a much smaller ratio. As mentioned in Section 2, we attribute these to stochastic magnitude variations leading to unphysical shapes of the observed phase curves.

[7] http://cdsweb.u-strasbg.fr/.

3.3. Suitability of H, G_{12}* for taxonomic classification using non-targeted observations

The different results between H, G_1, G_2 and H, G_{12}* are expected as the H, G_1, G_2 is more flexible due to the third photometric parameter. Muinonen et al. (2010) stress that the main advantage of the H, G_{12}-model with its reduced parameter space is its predictive power when utilized with sparsely-sampled phase curves. Indeed, giving non-targeted, sparse observations, and a prior knowledge on the target taxonomy, Penttilä et al. (2016) show that the absolute magnitude can be estimated using class-specific fixed slope parameters in the fitting procedure.

However, regarding a taxonomic classification based on the parameters of the H, G_{12}*-model, we conclude here that neither the absolute magnitudes nor the slope parameter are sufficiently reliable. The discrepancy between H and H_{12} prevents classification based on the absolute magnitude. To compare, we compute the colours of the asteroid taxonomic classes in the *Sloan Digital Sky Survey* (SDSS)[8] using the spectral templates of the classes from DeMeo and Carry (2013).[9] For each colour, we compute the average difference between the complexes, resulting in 0.03 mag (*u-g*), −0.03 mag (*g-r*), −0.04 mag (*r-i*), and 0.02 mag (*i-z*). The inaccuracies introduced by the H, G_{12}*-model are on average greater than these differences, preventing taxonomic classification. As outlined in Subsection 3.2, we regard the G_{12}*-parameter insufficient for any conclusion on the surface composition as well.

4. Taxonomy

In the following, we evaluate the taxonomic information content of the phase curve parameters, focusing on G_1, G_2-values derived from the serendipitous phase curves. We illustrate the distributions of the asteroid complexes and quantify their similarities in *cyan* and *orange*. Further evaluated are their wavelength-dependency and the ability to solve degeneracies of asteroid spectra using phase curve parameters.

The G_1, G_2- and G_{12}-distributions of different complexes have been studied by Oszkiewicz et al. (2011) and Shevchenko et al. (2016). We do not further explore the G_{12}*-parameter following the conclusion of Section 3.

4.1. Importance of observing the opposition effect

In a first iteration, we performed the following analysis on all acquired phase curves, using the limits on $\alpha_{\min}$, $\alpha_{\max}$, and N as outlined in Subsection 3.1. However, we noticed large dispersions in the arising G_1, G_2-distributions of the complexes, which showed a clear trend with respect to the number N of observations in each phase curve. G_1, G_2-parameters derived from phase curves with low N dispersed more from the center of the distributions than the ones from more densely covered phase curves.

The vital role of the opposition effect both for determining the absolute magnitude H and the taxonomic interpretation of the phase curve has been pointed out in the previous sections. Its non-linear dependence on the phase angle and the inherent magnitude dispersion of the serendipitous observations (refer to Section 6) require a dense coverage of observations to accurately describe the brightness surge. As ATLAS aims to observe asteroids on impact trajectory, only 7.3% of the 24 million observations analysed here have been acquired of asteroids at $\alpha \leq 3$deg., i.e. close to opposition, see Fig. B.1. For $N = 50$, this corresponds to 3–4 observations covering the most important part of the phase curve.

We therefore evaluated the trade off between dispersion introduced in G_1, G_2-space by phase curves with insufficient sampling of the opposition effect and by small sample numbers in less common asteroid taxa. Through visual inspection of the resulting complex distributions, we settled on $N = 125$ as limit for the following analyses, decreasing the initial sample size of 127,012 by more than half, down to 61,184. We stress that this large number of required observations stems from the science goal of the observatory providing the data; future large scale surveys like LSST can derive accurate phase curves from fewer observations provided the opposition effect is in the focus of the observation schedule.

4.2. Complex mapping

We retrieve previous taxonomic classifications from various references for 19,708 objects, in addition to reference albedo values for 14,384 of these classified asteroids. The albedos are employed to identify misclassifications and to separate classes into different complexes as outlined below. We collected these values from numerous sources and refer the reader to Appendix A and the online catalogue of the phase curve parameters for details.

The majority of classifications follow the Bus- or Bus-DeMeo-schemes (Bus and Binzel, 2002; DeMeo et al., 2009), which are performed on low-resolution asteroid reflectance spectra. As the phase curve parameters a priori contain less taxonomic information than spectra and to increase the size of the subsamples, we map the classes into broader taxonomic complexes. In the Bus-DeMeo taxonomy, there are 25 classes spanning a space of 13 complexes which are designated by unique letters of the alphabet (Binzel et al., 2019). We map the asteroids onto these complexes based on their previous classifications. For classes which have been defined in previous taxonomies but are no longer present in the Bus-DeMeo one, we choose the current complex resembling the previous class the most. As an example, the F-type defined in Tholen (1984) is mapped onto the B-complex.

Previous taxonomies like Tedesco et al. (1989) differentiate the X-type asteroids into low-albedo P-types, medium-albedo M-types, and high-albedo *E*-types. Asteroids with the same spectral shape but lacking albedo measurement are grouped into the X-types. As the albedo was dropped in subsequent taxonomies, so was the differentiation of the X-

Table 1
The applied mapping of asteroid taxa to complexes. The previous classifications are mapped to the complex denoted under Σ. N refers to the number of asteroids in each complex. $\bar{p}_V$ and σ_{p_V} give the mean visual albedo and its standard deviation respectively of all asteroids in the complex. The X-complex does contain asteroids with albedo measurements by definition.

Class		Σ	N	$\bar{p}_V$	σ_{p_V}
P, PC, PD, X, XC, XD, XL, Xc, Xe, Xk, Xt	→	P	593	0.05	0.02
D, DP	→	D	425	0.06	0.02
Cgh, Ch	→	Ch	266	0.06	0.06
B, F, FC	→	B	523	0.08	0.06
C, CB, CD, CF, CG, CL, CO, Cb, Cg, Cgx, Co	→	C	3670	0.09	0.09
T	→	T	62	0.12	0.06
M, X, XD, XL, Xc, Xe, Xk, Xt	→	M	660	0.15	0.05
K	→	K	586	0.18	0.09
L, LQ, Ld	→	L	776	0.19	0.09
O	→	O	5	0.21	0.10
S, SQ, SV, Sa, Sk, Sl, Sp, Sq, Sqw, Sr, Srw, Sv, Sw	→	S	8875	0.26	0.08
A, AQ	→	A	69	0.28	0.09
Q, QO, QV	→	Q	185	0.28	0.11
V, Vw	→	V	1412	0.36	0.11
E, X, XD, Xc, Xe, Xn, Xt	→	E	46	0.46	0.16
X, XD, XL, Xe, Xk, Xt	→	X	202	–	–

[8] https://www.sdss.org/.
[9] The template spectra are retrieved from http://smass.mit.edu/busdemeoclass.html.

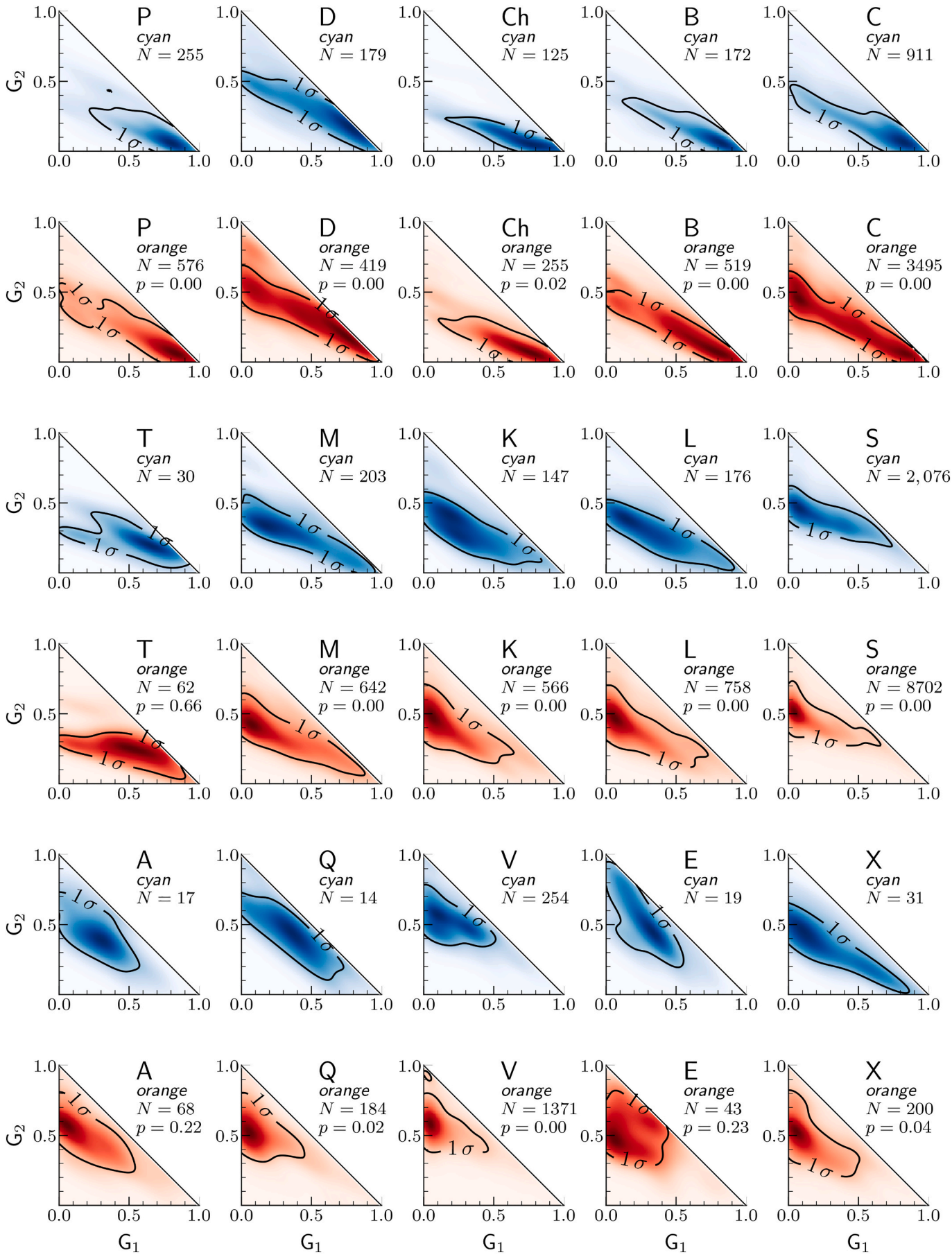

(caption on next page)

Fig. 6. Depicted are the G_1, G_2-distributions for several taxonomic asteroid complexes comprising 19,708 objects, derived from serendipitous phase curves observed by ATLAS in *cyan* and *orange*. The complexes are sorted in increasing order of their average visual albedo. The distributions are represented by 2 D Gaussian *kernel density estimators* (KDE) fitted to the G_1, G_2-pairs. The black contours give the KDE level at which 68% of the summed probabilities is encompassed, resembling the 1 σ-level of a Gaussian distribution. Further given are the number of asteroids N in each complex and waveband as well as the two-sample 2 D Kolmogorov-Smirnov p-values computed between the distributions in *cyan* and *orange* for each complex. (For interpretation of the references to colour in this figure legend, the reader is referred to the web version of this article.)

type classes. Given the correlation of the phase curve parameters with the albedo (e.g., Belskaya and Shevchenko, 2000; Penttilä et al., 2016; Belskaya and Shevchenko, 2018), we expect the X-type asteroids to separate in G_1, G_2-space. Therefore, we map asteroids classified in the X-complex into the P- ($p_V \leq 0.075$), M- ($0.075 < p_V < 0.30$), *E*- ($p_V \geq 0.30$), and X-complex (no reference albedo available), following the limits in Tholen (1984).

Hydrated C-types make up more than 30% of C-types in the Main Belt (Rivkin, 2012; Fornasier et al., 2014). The aqueous alteration is imprinted in absorption bands at 0.7- and 3.0 μm. The ATLAS *orange* filter covers the 0.7 μm band, therefore, these classes may separate in phase-parameter space. We split the Cgh- and Ch-types from the C-complex to investigate whether G_1, G_2 reveal the hydration.

The final mapping of classes to complexes is given in Table 1. Due to the low number of O-type asteroids, we exclude the complex from the analysis. We further rejected several ambiguous class assignments such as DS, CQ, SA, CS, XS from Carvano et al. (2010), which were performed on low-resolution visible photometry from the SDSS and given to objects which presented photospectra with different features in different observations. Further, the D-complex contains more than 200 objects with albedos between 0.1 and 0.5, indicating that they are misclassified. We therefore introduce an upper limit of 0.1 albedo on the D-type complex.

Finally, we exclude the Ad, Bk, Ds, and Kl classes from Popescu et al. (2018) temporarily. These classes are assigned based on near-infrared spectrophotometry using the VISTA-MOVIS catalogue (Popescu et al., 2016). The spectra of these types are degenerate in the regarded wavelength regime, therefore, the objects are classed together. The authors note that these classes are likely made up objects belonging to the denominating complexes (i.e. Ad is made up of A- and D-type asteroids). In a subsequent analysis step, we investigate the class ratios in these combinations using the phase curve parameters. We choose the VISTA-MOVIS sample rather than the SDSS sample by Carvano et al. (2010) as the degeneracy in near-infrared cannot be resolved without additional information such as the phase curve parameters. For the ambiguous SDSS results, additional observations in the visible could suffice to resolve the classifications.

4.3. Distribution of taxonomic complexes in G_1, G_2–space

The 2 D KDE distributions fitted to the G_1, G_2-parameters of the phase curves of the 15 complexes are shown in Fig. 6, both in *cyan* and *orange*, with a black contour marking the KDE level at which 68% of the summed probability is encompassed. The complexes are depicted in increasing order of their average visual albedo. It is readily apparent that the albedo-dependence of the opposition effect and photometric slope as described by Belskaya and Shevchenko (2000) is present in the ATLAS observations as well; with increasing average visual albedo, the distribution centers shift from large G_1-values towards medium- and finally large G_2 values, i.e. towards flatter phase curves and smaller opposition effects. We further find good agreement with the G_1, G_2-parameters extracted from targeted campaigns by Shevchenko et al. (2016) and Penttilä et al. (2016). The medium- and high-albedo S-, M-, and *E*-types populate regions of small photometric slopes, while low-albedo B-, C-, D-, and P-types present much larger slopes. Overall, the intermittent region around G_1=0.5 is sparsely populated; only the K- and T-complexes in both wavebands and the L-, and M-complexes in *cyan* present large probabilities there. We summarize the distributions in Table 2, giving the G_1, G_2-coordinates of the geometric center of the 95% probability-level contour for each complex. Further stated are the sizes of the areas encompassed by the 95%-probability contours, approximating the dispersion of the complexes in G_1, G_2-space after outlier rejection.

The strong disparity in the distributions of the E- and P-complexes shows that the phase coefficients present a reliable distinction between members of the X-complex, independent on reference albedo measurements. For the complexes where we discriminate based on on albedo, i.e. the P-, M-, E-, and D-type, we see large tails in the 1 σ-distributions, which we attribute to remaining misclassifications. Asteroid albedo measurements carry uncertainties around 17.5% (Masiero et al., 2018), suggesting that the P-, M-, and E-complexes are overlapping due to these interlopers. The C- and D-types present broad distributions, specifically in the *orange* samples. This indicates a substantial fraction of misclassifications in the literature. The majority of classifications is retrieved from visible photometry based on the SDSS. As noted in Subsection 4.2 and Carvano et al. (2010), asteroids can display ambiguous spectral features of several taxonomies, leading to mixing of high- and low-albedo classifications (misclassification of X- to C-types and S- to D-types). This hypothesis is further supported by the distribution of the Ch-complex. The classification of hydrated C-types is subject to more scrutiny than the more general C-types, hence we expect a much smaller fraction of misclassifications. Indeed, we observe less dispersed G_1, G_2-distributions in the lower-albedo regime for the Ch-complex. Finally, the contamination of the C-complex prevents a conclusion on the ability to observe hydration in slope parameter space.

We conclude that the parameters of phase curves carry substantial taxonomic information, even for serendipitously acquired observations. Several observational requirements need to be fulfilled, such as a dense coverage of the opposition effect. Nevertheless, this promises a classification dimension as insightful as the albedo while being more accessible to the observer.

4.4. Wavelength-dependency

Phase reddening describes the steepening of the spectral slope and a change in the bandwidths of asteroid spectra with increasing phase angle. The effect is non-linear, see Sanchez et al. (2012). As the asteroid spectra are phase-angle dependent, it follows that their phase curves in turn are wavelength-dependent, resulting in varying G_1, G_2-parameters. Carvano and Davalos (2015) investigate the phase-angle dependency of taxonomic classifications of asteroids in the visible wavelength-regime. They find that the taxonomic complexes are affected to different degrees; objects presenting the 1 μm-olivine/pyroxene-band show stronger correlations between spectral slope and phase angle than asteroids lacking the absorption feature.

The wavelength-dependency of the G_1, G_2-parameters is underlying to the question of whether it is admissible to combine observations acquired in different wavelength-regimes to overcome incomplete phase

Table 2
For each complex, we provide the number N of analysed phase curves as well as the geometric center C and area A of the 95%-probability contour in *cyan* (subscript c) and *orange* (subscript o). The areas are multiplied by 1000 for notation purposes. Further given are the photometric slope parameter k, the size of the opposition effect $\zeta - 1$, and the Kolmogorov-Smirnov p-values for each complex in this study. k and $\zeta - 1$ are calculated using the G_1, G_2-pairs of the geometric centers, following Eq. 6 and Eq. 7.

Σ	N_c	N_o	C_c	C_o	A_c	A_o	k_c	k_o	$\zeta - 1_c$	$\zeta - 1_o$	p
P	255	576	(0.80, 0.05)	(0.83, 0.06)	4.0	6.4	−1.82	−1.81	0.16	0.12	0.00
D	179	419	(0.77, 0.17)	(0.72, 0.20)	8.5	10.6	−1.67	−1.62	0.06	0.09	0.00
Ch	125	255	(0.77, 0.05)	(0.76, 0.07)	4.1	5.2	−1.84	−1.80	0.22	0.21	0.02
B	172	519	(0.82, 0.06)	(0.77, 0.08)	4.5	8.0	−1.82	−1.79	0.14	0.17	0.00
C	965	3609	(0.82, 0.06)	(0.83, 0.06)	6.2	5.0	−1.81	−1.82	0.13	0.13	0.00
T	30	62	(0.65, 0.19)	(0.53, 0.24)	6.3	7.5	−1.61	−1.49	0.18	0.29	0.66
M	203	642	(0.19, 0.34)	(0.07, 0.42)	9.0	7.5	−1.05	−0.77	0.92	1.02	0.00
K	147	566	(0.18, 0.40)	(0.06, 0.48)	8.6	6.6	−0.99	−0.72	0.71	0.87	0.00
L	176	758	(0.16, 0.37)	(0.06, 0.47)	9.0	6.7	−0.96	−0.73	0.89	0.89	0.00
S	2076	8702	(0.08, 0.46)	(0.04, 0.51)	6.4	3.5	−0.76	−0.67	0.87	0.81	0.00
A	17	68	(0.30, 0.39)	(0.05, 0.57)	7.5	6.2	−1.16	−0.68	0.46	0.60	0.22
Q	14	184	(0.36, 0.44)	(0.05, 0.52)	9.2	4.6	−1.18	−0.70	0.25	0.74	0.02
V	254	1371	(0.10, 0.56)	(0.04, 0.58)	6.5	3.2	−0.78	−0.67	0.50	0.60	0.00
E	19	43	(0.33, 0.45)	(0.06, 0.48)	8.0	8.8	−1.14	−0.73	0.29	0.86	0.23
X	31	200	(0.11, 0.45)	(0.06, 0.52)	9.0	5.6	−0.83	−0.70	0.81	0.73	0.04

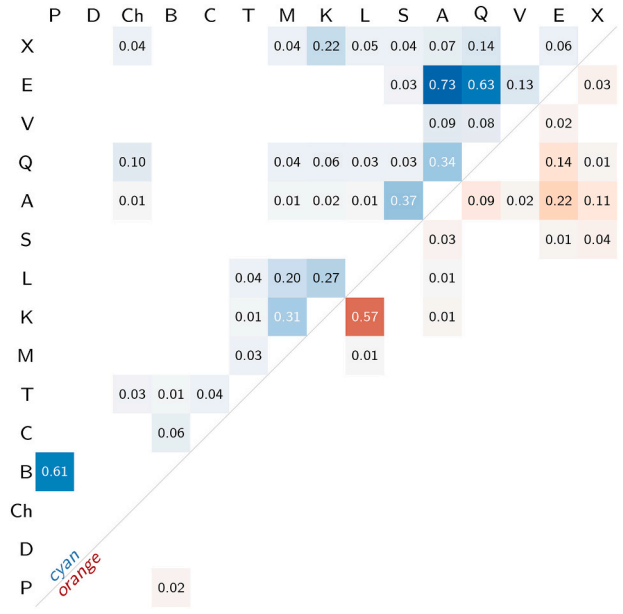

Fig. 7. The two-sample 2 D Kolmogorov-Smirnov p-values estimating the similarity between the observed G_1, G_2-pair distributions of the 15 asteroid taxonomic complexes in *cyan* (upper left) and *orange* (lower right). Values above 0.2 indicate that the two paired complexes may have the same underlying distribution in G_1, G_2-space. Values below 0.01 are not shown for readability. (For interpretation of the references to colour in this figure legend, the reader is referred to the web version of this article.)

curve coverage. Though the overlap of the ATLAS *cyan* and *orange* filters decreases the apparent wavelength-dependency (refer to Fig. 1), the dataset at hand offers a prime opportunity to investigate the dependency using similar asteroid samples, phase curve coverages, and apparent magnitude reduction pipelines.

We regard the G_1, G_2-distributions acquired in *cyan* and *orange* as two independent samples. The *Kolmogorov-Smirnov* (KS) p-value statistic evaluates the probability of the null hypothesis that the underlying distribution of the two compared samples is identical (Peacock, 1983). In general, provided the two compared samples are sufficiently large, p-values above 0.2 indicate a strong similarity, while values below 0.2 reject the null hypothesis. The results are given in Fig. 6 above the G_1, G_2-distribution *orange* of each complex as well as in Table 2. Most complexes present p-values equal or close to zero, i.e. they show wavelength-dependency. The A-, *E*-, and T-complex are above the 0.2-threshold. They are the three smallest samples, however, and their G_1, G_2-distributions are noticeably different. We therefore conclude that combining observations acquired in different wavebands should be strictly avoided. Additional support for the wavelength dependency of the phase curves can be derived from the Euclidean distance of the G_1, G_2-pairs in *cyan* and *orange* for objects observed in both bands. Computing the distances yields a distribution with mode at 0.127, in good agreement with the displacements of the complex centroid centers between the two wavebands given in Table 2.

Differences in the slopes of the phase curves observed at different effective wavelengths lead to spectral reddening which is proportional to the phase angle of observation. This is of particular importance for the ESA *Gaia* mission, which is scheduled to release asteroid spectra obtained at large solar elongation in its third data release in 2021 (Delbo et al., 2012). The acquired G_1, G_2-distributions describing the shapes of the phase curves allows us to quantify the amount of spectral reddening per degree phase angle for each taxonomic complex between the effective wavelengths of the *cyan* and *orange* bands. The spectral slope in units of %/100 nm is given by

$$S_S = \frac{f_o - f_c}{\lambda_o - \lambda_c} \cdot 10^4 \tag{11}$$

where f_c and f_o are the observed reflectance in *cyan* and *orange*, and $\lambda_c = 518\,\text{nm}$ and $\lambda_o = 663\,\text{nm}$ are the effective wavelengths. By relating the reflectances to the apparent magnitudes using the Pogson scale, we can express the spectral slope as

$$S_S = \frac{f_c\left(10^{-0.4(m_o - m_c)} - 1\right)}{\lambda_o - \lambda_c} \cdot 10^4 \tag{12}$$

Normalizing the reflectance at λ_c gives $f_c = 1$, and the remaining variable is the difference $m_o - m_c$, which we can derive using the phase

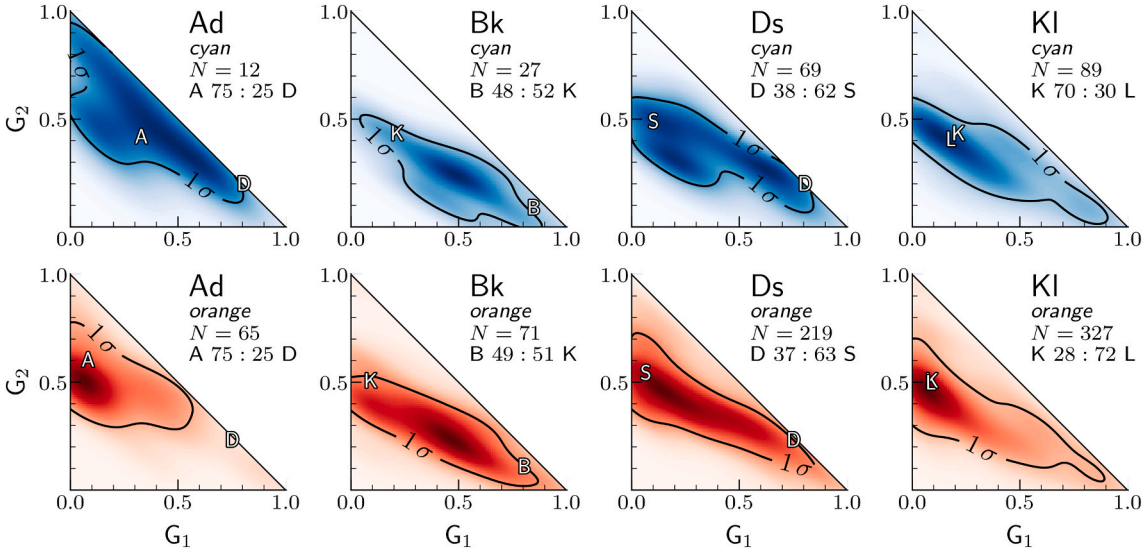

Fig. 8. Depicted are the G_1, G_2-distributions for four spectral classes from Popescu et al. (2018) containing two distinct asteroid taxa. The 2 D kernel density estimates of their G_1, G_2-distributions are shown for observations in *cyan* (blue) and *orange* (red). The black contour gives the 1 σ-level. The white letters denote the position of the asteroid complexes in G_1, G_2-space. *N* gives the number of asteroids in each sample, while the derived ratios of the principal classes are given below. (For interpretation of the references to colour in this figure legend, the reader is referred to the web version of this article.)

curves $m_c(\alpha)$ and $m_o(\alpha)$,

$$\Delta m = m_o\left(\alpha, H_o, G_{1,o}, G_{2,o}\right) - m_c\left(\alpha, H_c, G_{1,c}, G_{2,c}\right) \tag{13}$$

4.5. Identification of interlopers with G_1, G_2

The G_1, G_2-parameters offer an additional dimension to taxonomic classification, which is predominantly done in spectral space. The combination of both dimensions allows to identify interlopers and misclassifications.

Using the 2 D- KS statistic, we compute the *p*-values to quantify the resemblance of the asteroid taxa in G_1, G_2-space. In Fig. 7, we display the heatmap of the two-sample 2 D KS *p*-values quantifying the similarity of the distributions. The intersections on the upper left hand side compare the distributions in *cyan*, while the *orange* waveband comparison is depicted on the lower right hand side. The average visual albedo increases towards the upper right. Complex-combinations yielding *p*-values below 0.01 are left blank for readability.

Two trends are visible in the heatmap. First, high-albedo complexes tend to show more resemblance to each other than low-albedo complexes, where only the P- and B-complexes in *cyan* show strong likeness. Second, the complexes present larger *p*-values in *cyan*, where nine pairings cross the 0.2-threshold, prohibiting the rejection of the null hypothesis, as opposed to two pairs in *orange*. Both pairs, the K-, L- and the A-, E-complexes, cannot be distinguished in either waveband.

The degeneracies in phase curve parameter space appears reversed to the degeneracies in spectral feature space. High-albedo objects depict distinct absorption band properties in band depth, width, and wavelength, which allows for differentiation even in low-resolution data. Low-albedo types are separated based on their spectral slopes, which is in general less certain (Marsset et al., 2020). The phase parameters offer a complimentary classification space.

We apply this conclusion to four classes reported by Popescu et al. (2018) in the VISTA-MOVIS based classification. As outlined in subsection 4.2, the near-infrared photometry presents several degenerate classes, of which we show the G_1, G_2-pairs in Fig. 8. To estimate the ratios of the different taxa, we compute the distance in G_1, G_2-space for each object to the center coordinates of the complexes and assign the object to the complex it is closer to. This is a simple test and proper interloper identification should be performed accounting for the complete complex distributions; nevertheless, it is used as a proof of concept here. As we are working with center coordinates derived from statistical ensembles, we may misclassify single objects. However, the derived probabilities should hold for the entire samples.

The resolution of degeneracies is effective for the classes at opposite ends of the albedo spectrum, which here are the A-D- and D-S combinations. We retrieve the same ratios for both wavebands in these combinations, three-quarters of A-types in the former and about two-thirds of S-types in the latter.

For the Bk superposition, we observe almost identical ratios as well, while we note that the observed G_1, G_2-distribution peaks between the two complex centers. Properly accounting for the dispersion of the complexes in G_1, G_2-space might change the retrieved ratios considerably. The Kl class cannot be resolved as expected following Fig. 7.

Thus, we conclude that G_1, G_2-values derived from serendipitous observations are sufficient to untangle degeneracies arising in spectral feature space if the classes separate in albedo-space. Lower-albedo classes may even be separated from one another provided a reliable observation of the size of the opposition effect, which is the principal distinction between the B-, C-, D-, and P-types in G_1, G_2-space.

4.6. Distribution of taxonomic complexes in G_{12}*–space

Oszkiewicz et al. (2012) found the S-, C-, and X-types follow Gaussian distributions in G_{12}-space (rather than G_{12}*-space). Following the discussion in Section 3, we do not expect any reliable taxonomic

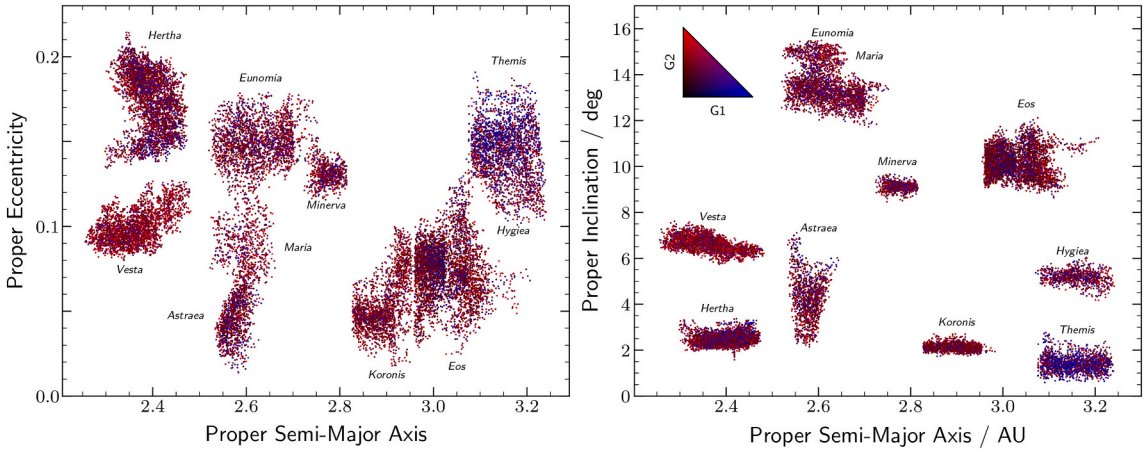

Fig. 9. Illustrated are the G_1, G_2-parameters of several asteroid families, plotted in proper orbital elements space as semi-major-axis versus eccentricity (top) and versus inclination angle (bottom). The phase curves were observed by ATLAS in *orange*. The proper orbital elements and family memberships are provided by AstDyS-2 (Milani et al., 2014). The colour-coding of the G_1, G_2-space for both figures is given in the inset of the right-hand plot.

Table 3
Asteroid families with the number N of members, the geometric centers C of the 95% probability-level contour, the area A of the 1 σ-contour, as observed by ATLAS in *cyan* (subscript c) and *orange* (subscript o). The areas A are multiplied by 1000 for notation purposes. Further given are the taxonomic classifications of the families and their references.

Family	N_c	N_o	C_c	C_o	A_c	A_o	Class	Reference
(4) *Vesta*	229	1647	(0.07, 0.50)	(0.04, 0.55)	162	106	V	Zappalà et al. (1990)
(5) *Astraea*	59	524	(0.11, 0.48)	(0.07, 0.48)	197	156	S	Huaman et al. (2017)
(10) *Hygiea*	101	473	(0.75, 0.11)	(0.08, 0.44)	191	184	C	Carruba (2013)
(15) *Eunomia*	383	1647	(0.11, 0.43)	(0.06, 0.49)	183	170	S	Nathues (2010)
(24) *Themis*	528	1218	(0.80, 0.05)	(0.73, 0.08)	96	151	C	Mothné-Diniz et al., 2005
(93) *Minerva*	114	539	(0.08, 0.49)	(0.07, 0.49)	159	170	S	Mothné-Diniz et al., 2005
(135) *Hertha*	264	1777	(0.36, 0.34)	(0.07, 0.49)	172	131	S	Dykhuis and Greenberg (2015)
(158) *Koronis*	502	1333	(0.06, 0.46)	(0.03, 0.52)	122	71	S	Tholen (1984)
(170) *Maria*	100	472	(0.19, 0.41)	(0.05, 0.47)	228	169	S	Zappalà et al. (1997)
(221) *Eos*	697	2732	(0.13, 0.36)	(0.04, 0.44)	174	134	K	Masiero et al. (2014)

information in the G_{12}*-distributions. However, for completeness, we show them analogously to Fig. 6 in Fig. C.2. Note that by definition, the D-, E-, and P-complexes cannot be modelled with H, G_{12}*, hence, we use a dashed linestyle for their distributions.

5. Asteroid families in phase space

In the following, we illustrate the use of the G_1, G_2 phase curve coefficients as an extension of the physical parameter space of families. We intend this as a proof-of-concept of the results in Section 4 rather than a full analysis of the implications.

The identification of asteroid families requires accurate parameter derivation and large number statistics to discern their members from the background of minor bodies (Milani et al., 2014). It is an interplay of their dynamical parameter space, specifically the proper orbital elements, and their physical parameters such as albedos and colours (Ivezić et al., 2002; Parker et al., 2008; Masiero et al., 2013)

The phase curve coefficients represent a large corpus of physical quantities when derived from serendipitous observations. Oszkiewicz et al. (2011) compute family-specific phase curves by fitting family members with constant G_1, G_2-parameters, minimizing a global χ^2 in a grid search and describing the quality of all fits simultaneously to arrive at the best fit for the family collective. The resulting G_1, G_2-values are concentrated towards medium photometric slopes and opposition effect sizes for all 17 families in the study, among which is the high-albedo (4) *Vesta* -family. We interpret this as indication that the simultaneous treatment of all family members suppresses the inherent information on family taxonomy and fraction of interlopers.

The distribution of family members in G_1, G_2-space can yield insights on the nature of their parent body or bodies. Unimodal distributions suggest a homogeneous taxonomy, e.g., from a homogeneous single parent body or from compositionally similar parent bodies of overlapping families. A heterogeneous taxonomy in either case would give rise to multimodal distributions in G_1, G_2-space, as would the presence of a considerable fraction of interlopers. Finally, the superposition of distinct families in orbital space could be reflected in their phase coefficients in the case of different taxonomic nature.

We retrieve the proper orbital elements (semi-major axis a_p, eccentricity e_p, and orbital inclination angle i_p, refer to Milani and Knežević (1992); Knezevic and Milani, 2000) for 93,200 asteroids observed by ATLAS as well as their family memberships from the *Asteroids - Dynamic Site 2* (AstDyS-2)[10] (Milani et al., 2014). We select all families of which more than 500 members have been observed by ATLAS, either in *cyan* or in *orange*, after applying the limit of $N \geq 150$ on the sample from Section 3. 10 families pass the required number of observed members: (4) *Vesta*, (5) *Astraea*, (10) *Hygiea*, (15) *Eunomia*, (24) *Themis*, (93) *Minerva*, (135) *Hertha*, (158) *Koronis*, (170) *Maria*, and (221) *Eos*.[11] The distributions of the families in $a_p - e_p$- and $a_p - i_p$-space are shown in Fig. 9. Each dot

[10] https://newton.spacedys.com/astdys2/.

[11] Note that the (8) *Flora* family is not present in `AstDyS-2` as it does not differentiate sufficiently from the background in the hierarchical clustering method used, see Milani et al. (2014).

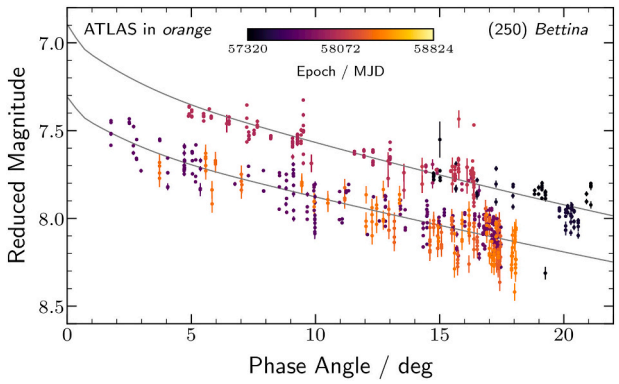

Fig. 10. The phase curve of (250) *Bettina* as observed by ATLAS in *orange*. The observations are colour-coded by their epoch, highlighting the four different apparitions that were captured. The triaxial ellipsoid ratios of (250) *Bettina* are 1.4:1:1 (Viikinkoski et al., 2017). The gray lines show the H, G_1, G_2-model fits to the apparitions, split into pairs of two.

represents an asteroid, colour-coded by its G_1, G_2-values. The illustrated sample is restricted to phase curves observed in *orange* to show the larger subsample while eliminating the wavelength-dependency. We quantify the G_1, G_2-distributions for the families as done in Section 4 for the taxonomic complexes. The 2 D KDEs are depicted in Fig. D.3, split into *cyan* and *orange*. We summarize them in Table 3, giving the area of the 1 σ-contour and the geometric center of the 95% probability-level contour. The former is indicative of the fraction of interlopers or the taxonomic heterogeneity of the parent bodies, while the latter characterizes the G_1, G_2-values of the core family members. In addition, we state reference taxonomic classifications of the families.

Three families show strong uniformity, both visually in Fig. 9 and in their small area sizes in Table 3. (4) *Vesta* is the archetype of the high-albedo taxonomic class, the V-types (Zappalà et al., 1990), in agreement with the large G_2 values of its core member center positions.

(24) *Themis* is a C-type family with known low-albedo interlopers such as the B-type subfamily (656) *Beagle* (Mothé-Diniz et al., 2005; Fornasier et al., 2016). While in *cyan* these complexes appear indistinguishable, the blue B-types separate from the red C-types towards the *orange* wavelength-regime, refer to Table 2. We are not able to resolve this shift using the classified B- and C-types in the (24) *Themis* family subsample, nevertheless, phase curves from targeted observations might detect this difference (Shevchenko et al., 2016).

(158) *Koronis* is one of the largest families in terms of number and we confirm here its homogeneous S-type taxonomy (Tholen, 1984).

The C-type family (10) *Hygiea* shows a considerable fraction of objects with high albedos in *cyan*, as well as objects with high albedos in *orange*. Carruba (2013) have identified S- and X-type interlopers in the family. We further attribute this partially to remaining phase curves with insufficient opposition effect coverage, as the distribution shifts towards C-type objects with increasing N.

The C-type asteroid (93) *Minerva* is the namesake of an S-type family (Mothé-Diniz et al., 2005).

We note that the family centers given in Table 3 are not compatible with the results of Oszkiewicz et al. (2011); the geometric centers of the families extend more towards the upper G_1- and G_2-values as seen by Penttilä et al. (2016). We attribute this to our treatment of each family member separately, allowing for a differentiated look into the G_1, G_2-distributions, specifically separating the core family members and potential interlopers.

As in Subsection 4.5, we conclude here that the G_1, G_2-space is well suited for interloper detection, adding a physical parameter space to asteroid families that can confirm dynamical identification and strengthen the definition of families. This, in turn, improves their age estimates (Spoto et al., 2015).

6. Error sources in serendipitous phase curves

Reduced phase curves from targeted campaigns are available for in the order of 100 asteroids. To increase the number of asteroids with available phase coefficients, exploiting serendipitous asteroid observations is necessary. The uncertainty σ of the reduced magnitudes in serendipitous phase curves is a propagation of uncertainties arising from their 3 D-shape and from the observational parameters themselves,

$$\sigma \propto \sqrt{\sigma_{\mathrm{PHOT}}^2 + \sigma_{\mathrm{PREC}}^2 + \sigma_{\mathrm{SYS}}^2 + \sigma_{\mathrm{ROT}}^2 + \sigma_{\mathrm{APP}}^2} \tag{14}$$

where σ_{PHOT} is the photometric uncertainty of a single observation, σ_{PREC} refers to the loss in precision when magnitudes are reported in a truncated format, σ_{SYS} is introduced by varying photometric systems used either in different observatories or by an observatory over time, and σ_{ROT} and σ_{APP} are magnitude modulations introduced by the asteroid's shape, specifically the asteroid's rotation and the change in aspect angle over different apparitions respectively. These uncertainties, disperse the observed reduced magnitudes, leading to broader posterior distributions (i.e. uncertainties) of the phase curve parameters as seen in Fig. 3. Eq. 14 is a non-exhaustive list, though the dominating error sources are encompassed.

Following the discussions in Section 3 and Section 4, the coverage of the opposition effect further affects the derived H, G_1, G_2-parameters. As opposed to the factors in Eq. 14, its impact can be minimized by a carefully set observation schedule.

In the following, we examine the order of magnitude of each uncertainty listed in Eq. 14 and different degrees of coverage of the opposition effect, intending to identify the dominating uncertainty and means to minimize it.

6.1. Photometric uncertainty and precision

In the most basic form, any observed magnitude carries an uncertainty e.g. due to random photon noise. These cannot be avoided and are present also in targeted campaigns. In the ATLAS observations, the mean photometric error is 0.14 mag, with a standard deviation of 0.08 mag depending largely on the apparent magnitude of the target. The LSST aims at $\sigma_{\mathrm{PHOT}} \sim 0.01$ mag for single exposures of objects with a magnitude in r of 21 (LSST Science Collaboration, 2009).

When working with serendipitous observations, however, this precision is frequently truncated to 0.1 mag either when the observations are reported to or retrieved from the MPC. This adds an uncertainty of $\sigma_{\mathrm{PREC}} = 0.1/\sqrt{12}$ mag on top of σ_{PHOT}, where the $\sqrt{12}$ divisor comes from the standard deviation of the uniform distribution. Once the new data pipeline accepting the updated observation report format has been put into place by the MPC, this source of error will be removed (Chesley et al., 2017).

6.2. Photometric systems

There are systematic magnitude offsets which have to be taken into account when combining magnitudes observed by different observatories, or even data from a single observatory which underwent recalibration. A more in-depth look is done by Oszkiewicz et al. (2011). The differences in the photometric systems are not always apparent, e.g. when retrieving observations from the MPC.

As a baseline estimation of σ_{SYS}, we use the example of the SDSS and Pan-STARRS systems. Both share the *g*, *r*, *i*, and *z* filters, though there are slight differences in their throughputs. Computing the average differences in apparent magnitude of the mean spectra for the 24 taxonomic classes in (DeMeo et al., 2009) gives σ_{SYS} values of 0.09 mag, 0.01 mag, 0.02 mag, and 0.08 mag for the four filters respectively. For bright asteroids, this is in the order of σ_{PHOT}.

In Subsection 4.1, we highlight the importance of densely sample phase curves. We see here that achieving a large number of observations by combining data from different photometric systems is a trade-off between increased phase curve coverage and introduced dispersion in apparent magnitude.

6.3. Asteroid rotation and apparition effect

The light curve of an asteroid is modulated by to its 3 D-shape rotating around its spin axis. The rotation imprints a periodic modulation of the apparent magnitude over the rotation period, which is typically in the order of a few hours (Warner et al., 2009).[12] In addition, the varying aspect angles over different apparitions of the asteroid introduce offsets in the observed magnitude, effectively shifting the whole phase curve along the *y*-axis, hence biasing the determination of the absolute magnitude *H*.

Fig. 10 shows an example of both effects affecting the phase curve of (250) *Bettina*, as observed by ATLAS in *orange*. The epoch of observation is colour-coded. Four distinct apparitions can be seen in the observations, leading to shifts in the reduced magnitudes which give the impression of two superimposed phase curves being displayed. On top of the apparition effect, we see the magnitude dispersion within the apparitions, introduced in part by the asteroid's spin.

The strength of the magnitude modulation due to rotation and change in aspect angle depend on the shape of the asteroids and the viewing geometry. The *Database of Asteroid Models from Inversion Techniques* (DAMIT)[13] provides shape models for 2407 asteroids (Durech et al., 2010). We use these shape models to quantify the effect of the rotational modulation (σ_{ROT}) and of the varying aspect angle (σ_{APP}).

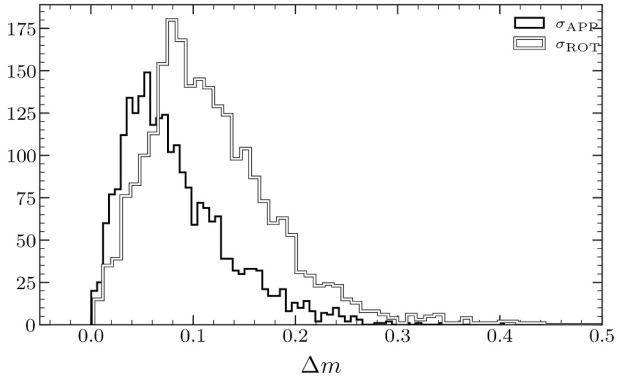

Fig. 11. The amplitude of magnitude dispersion due to the asteroids' rotation (black) and change in aspect angle between different apparitions (white). The values are derived using the DAMIT shape models from Durech et al. (2010).

Table 4
The distributions of the differences between the 100 phase curves with simulated noise (σ) and the *H*, G_1, G_2-parameters of the targeted (20) *Massalia* observations by Gehrels (1956). The same is given for the truncated ATLAS phase curves, with *i* deg. describing the dropout degree. μ refers to the mean values of the distributions, while σ gives the median of the absolute differences.

	μ_{Δ_H}	σ_{Δ_H}	$\mu_{\Delta_{G1}}$	$\sigma_{\Delta_{G1}}$	$\mu_{\Delta_{G2}}$	$\sigma_{\Delta_{G2}}$
σ	0.04	0.11	0.07	0.08	−0.01	0.10
1 deg	0.00	0.07	−0.00	0.04	0.01	0.01
2 deg	−0.00	0.12	−0.01	0.07	0.01	0.02
3 deg	−0.01	0.15	−0.02	0.09	0.02	0.03
4 deg	−0.00	0.18	−0.03	0.09	0.03	0.03
5 deg	0.02	0.21	−0.03	0.10	0.05	0.05

For each asteroid, we compute its triaxial dimensions ($a > b > c$) and assimilate its shape to a smooth ellipsoid in the following. Under this assumption, the modulation of the apparent magnitude due to spin and 3D shape writes

$$m = -2.5log(\pi abc \cdot \left(\left(\frac{cos\beta cos\lambda}{b}\right)^2 + \left(\frac{cos\beta sin\lambda}{a}\right)^2 + \left(\frac{sin\beta}{c}\right)^2\right)^{0.5}) \quad (16)$$

with λ, β being the longitude and latitude of the subobserver point (Surdej and Surdej, 1978; Ostro and Connelly, 1984).

We generate a full-rotation synthetic light curve every 10 days over an entire orbital revolution around the Sun, effectively probing the range of Sun-target-observer geometries. As serendipitous observations randomly occur over the rotation period, the measured magnitude is

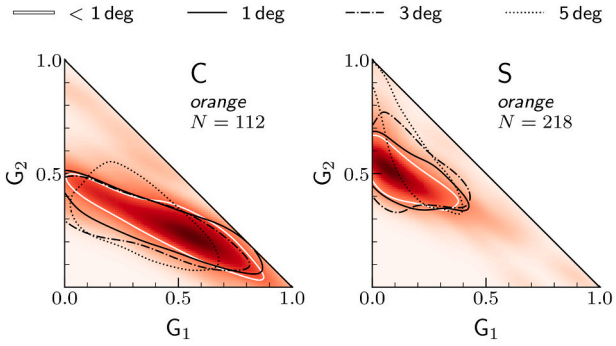

Fig. 12. The effect of insufficient phase curve coverage at low angles on the G_1, G_2-parameters. Shown are the 2 D fitted kernel density estimators of the G_1, G_2-distribution for C-type and S-type asteroids (red). The solid white line displays the 1 σ-level of the distribution using the complete ATLAS phase curves, the black solid, dash-dotted, and dotted contours the distributions using the phase curves truncated at 1 deg., 3 deg., and 5 deg. respectively. (For interpretation of the references to colour in this figure legend, the reader is referred to the web version of this article.)

[12] http://alcdef.org/.

[13] http://astro.troja.mff.cuni.cz/projects/damit.

offset from the average value. We estimate this offset σ_{ROT} by computing the root mean square residuals of each light curve to its average.

The influence of the varying aspect angle is computed from the difference σ_{APP} between the average magnitude of each light curve and a light curve taken while the observer is located within the equatorial plane of the asteroid.

The distributions of the changes in apparent magnitude for both effects are shown in Fig. 11. σ_{ROT} is in general larger than σ_{APP}, with a median value of 0.11 mag compared to 0.07 mag respectively. For σ_{APP}, the situation is analogous to σ_{SYS}; it can be removed by avoiding the combination of observations from different apparitions of the target. Nevertheless, the benefits of adding more samples of the phase curve may outweigh the downsides of increased magnitude dispersion. In Fig. 10, the parameter inference failed when applied to all observations, while we could retrieve two phase curves of (250) *Bettina* after splitting the apparitions in pairs of two.

6.4. Effect of magnitude dispersion on H, G_1, G_2

To quantify how the magnitude dispersion due to the uncertainties listed in Eq. 14 affect the H, G_1, G_2-model parameters, we simulate the (20) *Massalia* phase curve by Gehrels (1956) in Fig. 2 as serendipitous observations. Using the order of magnitudes for the uncertainties derived above ($\sigma_{\mathrm{PHOT}} = 0.1$ mag, $\sigma_{\mathrm{PREC}} = 0.1/\sqrt{12}$ mag, $\sigma_{\mathrm{SYS}} = 0.05$ mag, $\sigma_{\mathrm{ROT}} = 0.11$ mag, and $\sigma_{\mathrm{APP}} = 0.07$ mag), we compute the propagated uncertainty and simulate 100 phase curves of (20) *Massalia* with $N = 6$ at the same phase angles as the original observations, but randomly displaced following a Gaussian distribution with the mean value of the original magnitude observed at the respective phase angle and the standard deviation of the propagated uncertainty σ.

For these 100 phase curves, we compute the H, G_1, G_2-parameters and the differences to the parameters of the original phase curve,

$$\Delta\Theta = \Theta_i - \Theta, \quad \mathrm{i} \in \{1, \ldots, 100\} \tag{17}$$

where Θ refers to the H, G_1, G_2-parameters. The mean difference and the median value of the absolute difference of the resulting distributions are given in the first row of Table 4. The former indicates systematic parameter shifts with respect to the original values, while the latter indicates the spread of the differences. We choose the median rather than the standard deviation to be able to compare the results to the non-Gaussian distributions we obtain in the next subsection.

The simulated phase curves on average show larger H and G_1, i.e. they are steeper while depicting smaller opposition effect sizes. While the opposition effect in the original observations is sampled sufficiently, the stochastic nature of the simulated observations is reflected in the large median values of the absolute differences of all three parameters. This highlights the need for dense sampling to allow for restricting the parameter space; the offset in $\mu\Delta H$ in the simulated phase curves renders taxonomic classification from the computed colours inconclusive.

6.5. Opposition effect coverage

When relying on serendipitous asteroid observations, the coverage of the opposition effect is pre-determined by the survey footprint. This dependence of the scientific yield in terms of asteroid phase curves, colours, or taxonomies on the solar elongation coverage should be taken into account early on.

To quantify the influence of insufficient phase angle coverage, we select all ATLAS phase curves in *cyan* and *orange* with $\alpha_{\mathrm{min}} \leq 1$ deg. and $N \geq 50$ of asteroids with shape models present in DAMIT. 917 phase curves of 720 asteroids fulfill these criteria. Next, we reduce the spin- and apparition-induced magnitude dispersion in the phase curves using shape models and the light curve generation software[14] provided by DAMIT. This increases the probability that in the following simulations, we observe the influence of the opposition effect coverage rather than the magnitude dispersion on the H, G_1, G_2-parameters. However, the photometric noise cannot be removed by essence and some residuals arise from the non-ideal fit of the photometry by the shape-induced light curve.

The mean minimum phase angle of the reduced subset is 0.6 deg. We remove observations below {1, 2, 3, 4, 5} deg. phase angle and compute the H, G_1, G_2-model fit. The relevance of the opposition effect can then be quantified by looking at the difference of the H, G_1, G_2-parameters of the complete and the truncated phase curves. In Table 4, we display the difference in the parameters of the truncated phase curves and the complete phase curves, defined analogously to Eq. 17 with i referring to the truncation angle. With diminishing coverage of the opposition effect, the error on H increases up to 0.2 mag in these simulations. Following Eq. 2, this translates to an error of 17% on the derived asteroid albedo. Further, we observe systematic shifts of the G_1, G_2 parameters. We display this in Fig. 12, depicting the G_1, G_2-distributions for 112C-types and 218 S-types observed in *orange*. The contours depict the 1 σ-outlines for the complete phase curves (white), and increasing truncation angle (black). As the angle increases, the taxonomic information gets lost.

7. Conclusion

We perform phase curve parameter inference using serendipitous asteroid observations for a large number of minor bodies. The ATLAS observatory provided us with dual-band photometry for more than 180,000 objects, of which we selected about 95,000 based on the sampling statistics of their phase curves. As ATLAS continues to survey the night sky, we will be able to add an increasing number of asteroids to this analysis.

Our results show that the H, G_1, G_2-model parameters contain significant taxonomic information of the target surface, provided the opposition effect is densely sampled. The close correlation between the G_1, G_2-parameters and the albedo allows to use serendipitously observed phase curves as accessible albedo proxy for hundreds of thousands of asteroids with the upcoming LSST and NEOSM surveys. The taxonomic complexes separate sufficiently in the phase-coefficient space to study ensembles of asteroids such as asteroid families, while the large tails of the distributions prevent classification of single objects from G_1, G_2 alone.

We find evidence for a wavelength-dependency of the phase coefficients. Provided the taxonomy is known, the derived slope parameters of the complexes allow for estimating the degree of phase reddening in the slopes of asteroid spectra.

We quantified the sources of uncertainties of serendipitously acquired phase curves and their effect on the G_1, G_2 parameters. By simulating incomplete phase curves at low phase angles, we highlight the importance of observations close to opposition (≤ 1 deg) to determine the fundamental absolute magnitude H, used to derived properties such as albedo, colours, and taxonomic class.

[14] https://astro.troja.mff.cuni.cz/projects/damit/pages/software_download.

Declaration of Competing Interest

None.

Acknowledgements

This work has made use of data from the Asteroid Terrestrial-impact Last Alert System (ATLAS) project. ATLAS is primarily funded to search for near earth asteroids through NASA grants NN12AR55G, 80NSSC18K0284, and 80NSSC18K1575; byproducts of the NEO search include images and catalogues from the survey area. The ATLAS science products have been made possible through the contributions of the University of Hawaii Institute for Astronomy, the Queen's University Belfast, the Space Telescope Science Institute, and the South African Astronomical Observatory.

This research has made use of IMCCE's Miriade VO tool.

This research has made use of the SVO Filter Profile Service supported from the Spanish MINECO through grant AYA2017-84089.

Appendix A. Online catalogue

We briefly describe the structure of the online catalogue submitted to the CDS of phase curve parameters. The results are provided in a CSV-formatted table consisting of 127,012 rows, with each row providing the parameters of a single asteroid in a single ATLAS observation band. About a third of the asteroids appear in twice, once for *cyan* and once for *orange*. The column names and brief descriptions are given in Table A.1. For 43 H, G_1, G_2-model fits, no MCMC sample was withing the physical range of the G_1, G_2-parameters. These fits are considered failed and the parameters are empty in the catalogue provided online.

Table A.1
Structure of the online catalogue providing the phase curve parameters.

Column	Description	Column	Description
Number	Asteroid number	rms12	RMS of H, G_{12}*-model fit
Name	Asteroid name or designation	h_up	Upper 95% HDI value of H
Band	ATLAS observation band, either *cyan* or *orange*	h_low	Lower 95% HDI value of H
Class	Reference taxonomic classification for	g1_up	Upper 95% HDI value of G_1
scheme	Taxonomic scheme of reference	g1_low	Lower 95% HDI value of G_1
ref_tax	Code to identify taxonomy reference	g2_up	Upper 95% HDI value of G_2
ap	Proper semi-major-axis from AstDyS-2	g2_low	Lower 95% HDI value of G_2
ep	Proper eccentricity from AstDyS-2	h12_up	Upper 95% HDI value of H_{12}
ip	Proper inclination from AstDyS-2	h12_low	Lower 95% HDI value of H_{12}
N	Total number of observations	g12_up	Upper 95% HDI value of G_{12}*
phmin	Minimum phase angle of observations	g12_low	Lower 95% HDI value of G_{12}*
phmax	Maximum phase angle of observations	albedo	Reference albedo
h	Fitted H of H, G_1, G_2-model	err_albedo	Uncertainty of reference albedo
g1	Fitted G_1 of H, G_1, G_2-model	ref_albedo	Code to identify albedo reference
g2	Fitted G_2 of H, G_1, G_2-model	family_number	Family number from AstDyS-2
rms	RMS of H, G_1, G_2-model fit	family_name	Family name from AstDyS-2
h12	Fitted H_{12} of H, G_{12}*-model	family_status	Family status from AstDyS-2
g12	Fitted G_{12}* of H, G_{12}*-model		

Appendix B. Observation bias towards large phase angles for impactor detection

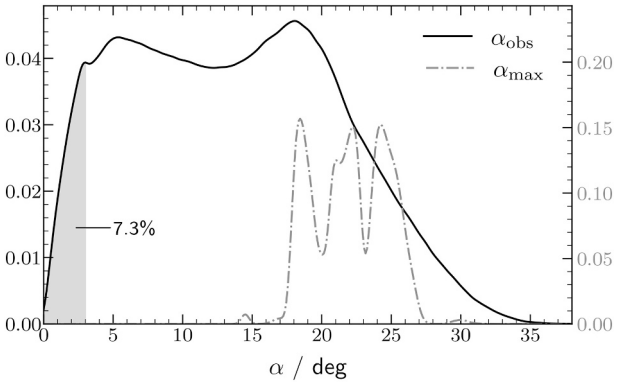

Fig. B.1. The black line shows the kernel density estimation of the distribution of asteroid phase angles at the epoch of observations, for all 20.7 million ATLAS observations analysed in this work. We further show the kernel density estimation of the distribution of the maximum observable phase angles of all asteroids in the sample, derived from their proper semi-major axis a_p as $\alpha_{max} = 2/\sin^{-1}(1/(2a_p))$.

Appendix C. G_{12}* of taxonomic complexes

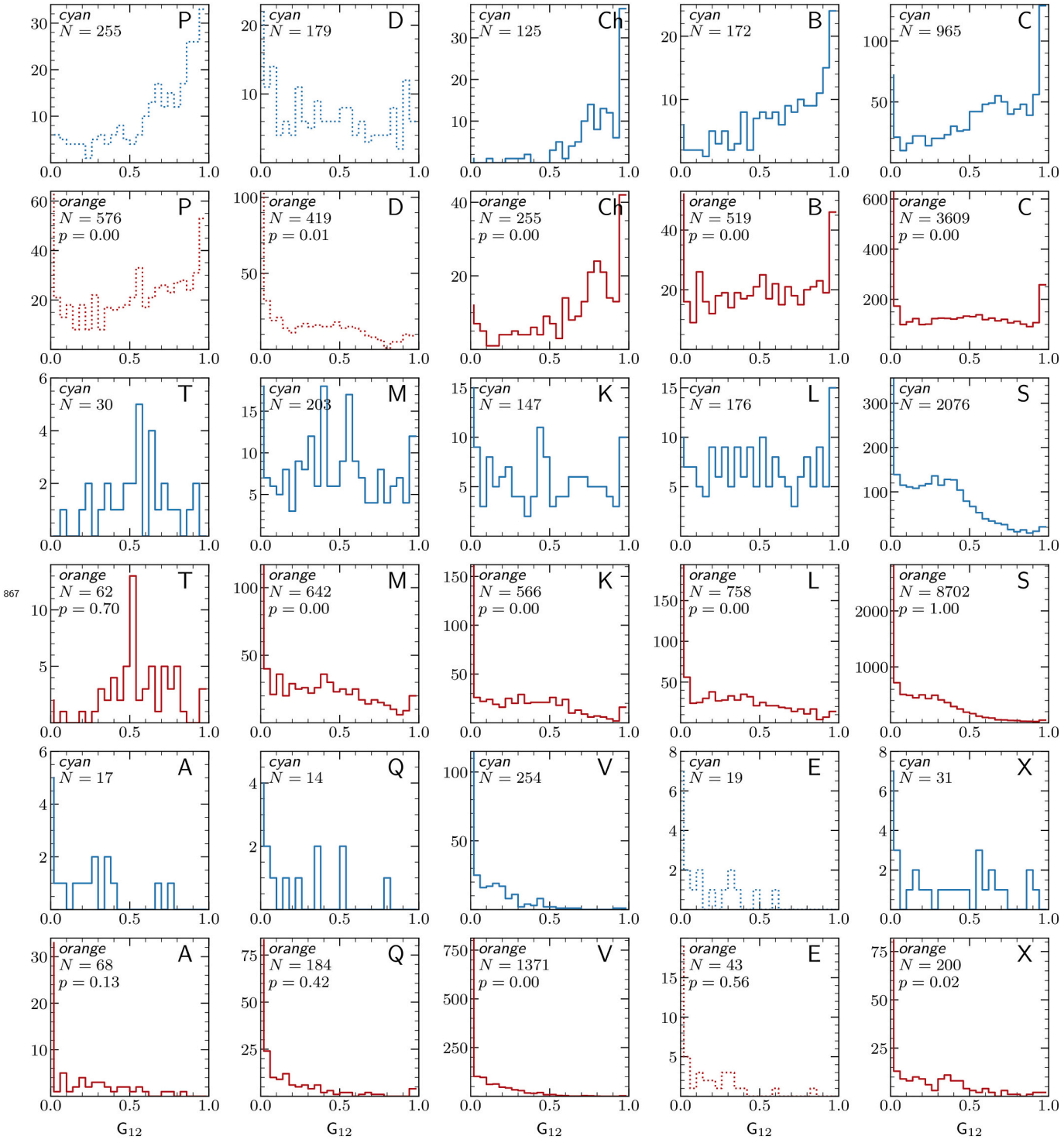

Fig. C.2. The G_{12}*-distributions for several taxonomic complexes of asteroids, derived from serendipitous observations by ATLAS in *cyan* and in *orange*. We give the sample sizes *N* and the two-sample Kolmogorov-Smirnov *p*-value between the *cyan* and *orange* G_{12}*-distributions of the complexes. The *H*, G_{12}*-model is not suited for the D-, *E*-, and P-complexes, hence they are displayed with a dotted linestyle. (For interpretation of the references to colour in this figure legend, the reader is referred to the web version of this article.)

Appendix D. G_1,G_2 of families

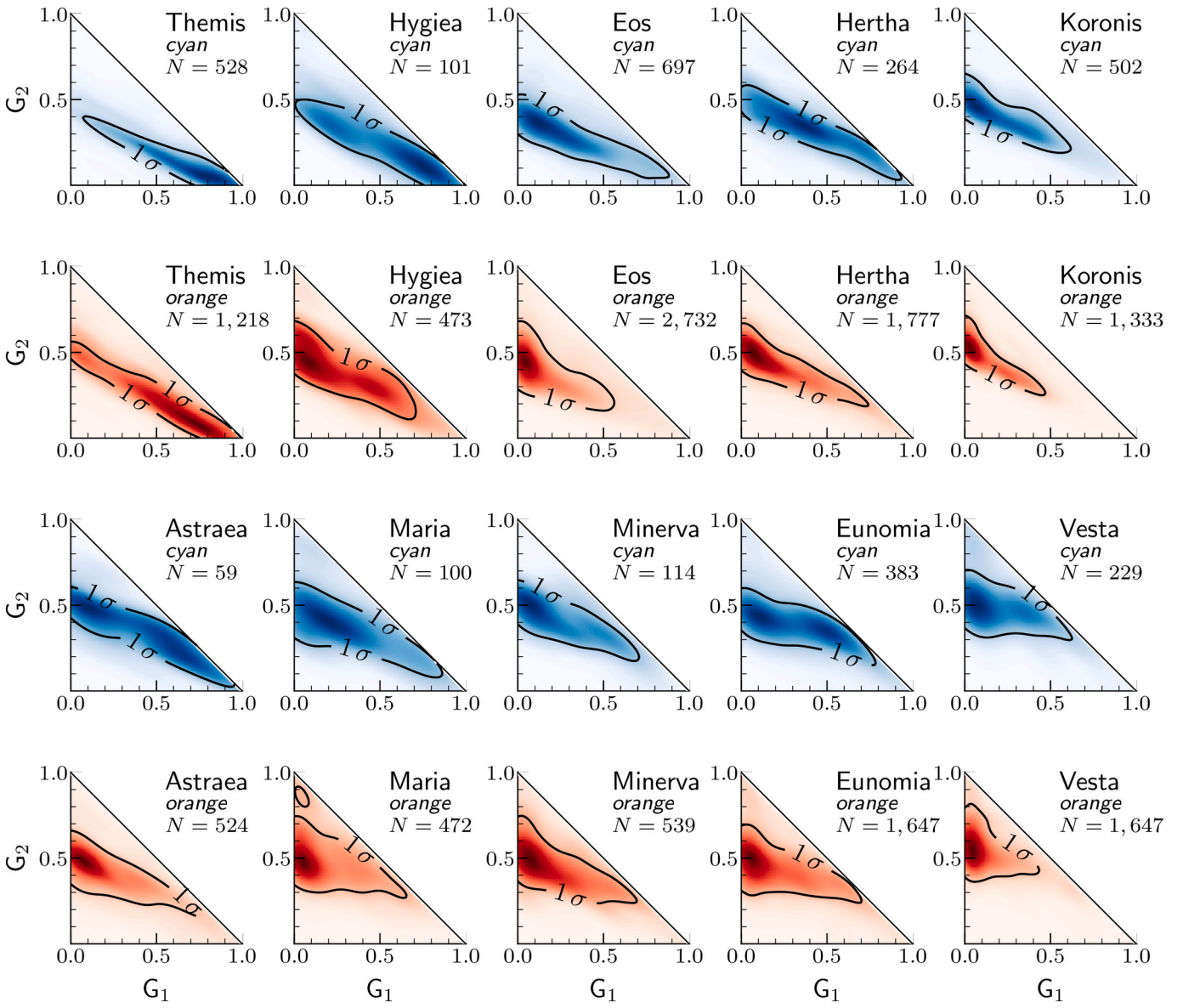

Fig. D.3. Depicted are the G_1, G_2-distributions of the members of 10 asteroid families observed by ATLAS in *cyan* (blue) and *orange* (red). The black contours illustrate the 1 σ-levels of the fitted 2 D kernel density estimators. The number of phase curves in each family and band is given by *N*. (For interpretation of the references to colour in this figure legend, the reader is referred to the web version of this article.)

References

Belskaya, I., Shevchenko, V., 2000. Opposition effect of asteroids. Icarus 147, 94–105. URL: https://doi.org/10.1006/icar.2000.6410.

Belskaya, I., Shevchenko, V., 2018. Phase angle effects in brightness and polarization for different classes of small solar system bodies. In: European Planetary Science Congress, pp. EPSC2018–730.

Berthier, J., Hestroffer, D., Carry, B., Durech, J., Tanga, P., Delbo, M., Vachier, F., 2008. A service of position and physical ephemerides computation dedicated to the small bodies of the solar system. In: Asteroids, Comets, Meteors, 2008, p. 8374.

Binzel, R., DeMeo, F., Turtelboom, E., Bus, S., Tokunaga, A., Burbine, T., Lantz, C., Polishook, D., Carry, B., Morbidelli, A., Birlan, M., Vernazza, P., Burt, B., Moskovitz, N., Slivan, S., Thomas, C., Rivkin, A., Hicks, M., Dunn, T., Reddy, V., Sanchez, J., Granvik, M., Kohout, T., 2019. Compositional distributions and evolutionary processes for the near-earth object population: results from the mit-Hawaii near-earth object spectroscopic survey (mithneos). Icarus 324, 41–76. https://doi.org/10.1016/j.icarus.2018.12.035.

Bowell, E., Hapke, B., Domingue, D., Lumme, K., Peltoniemi, J., Harris, A.W., 1989. Application of photometric models to asteroids. In: Binzel, R.P., Gehrels, T., Matthews, M.S. (Eds.), Asteroids II, pp. 524–556.

Bus, S., Binzel, P., 2002. Phase ii of the small main-belt asteroid spectroscopic survey a feature-based taxonomy. Icarus 158, 146–177. https://doi.org/10.1006/icar.2002.6856.

Carruba, V., 2013. An analysis of the hygiea asteroid family orbital region. In: Monthly Notices of the Royal Astronomical Society, 431, pp. 3557–3569. https://doi.org/10.1093/mnras/stt437.

Carry, B., 2018. Solar system science with esa Euclid. Astron. Astrophys. 609, A113. https://doi.org/10.1051/0004-6361/201730386.

Carvano, J.M., Davalos, J.A.G., 2015. Shape and solar phase angle effects on the taxonomic classification of asteroids. A&A 580, A98. https://doi.org/10.1051/0004-6361/201526268.

Carvano, J.M., Hasselmann, P.H., Lazzaro, D., Mothé-Diniz, T., 2010. Sdss-based taxonomic classification and orbital distribution of main belt asteroids. Astron. Astrophys. 510, A43. https://doi.org/10.1051/0004-6361/200913322.

Chesley, S.R., Hockney, G.M., Holman, M.J., 2017. Introducing ades: a new iau astrometry data exchange standard. In: AAS/Division for Planetary Sciences Meeting Abstracts, p. 112.14.

Delbo, M., Gayon-Markt, J., Busso, G., Brown, A., Galluccio, L., Ordenovic, C., Bendjoya, P., Tanga, P., 2012. Asteroid spectroscopy with gaia. Planet. Space Sci. 73, 86–94. https://doi.org/10.1016/j.pss.2012.07.029.

DeMeo, F., Carry, B., 2013. The taxonomic distribution of asteroids from multi-filter all-sky photometric surveys. Icarus 226, 723–741. https://doi.org/10.1016/j.icarus.2013.06.027.

DeMeo, F.E., Binzel, R.P., Slivan, S.M., Bus, S.J., 2009. An extension of the bus asteroid taxonomy into the near-infrared. Icarus 202, 160–180. URL: https://api.elsevier.com/content/article/PII:S0019103509000554?httpAccept=text/plain. https://doi.org/10.1016/j.icarus.2009.02.005.

Durech, J., Sidorin, V., Kaasalainen, M., 2010. Damit: a database of asteroid models. A&A 513, A46. https://doi.org/10.1051/0004-6361/200912693.

Dykhuis, M.J., Greenberg, R., 2015. Collisional family structure within the nysa–polana complex. Icarus 252, 199–211. https://doi.org/10.1016/j.icarus.2015.01.012.

Erasmus, N., Navarro-Meza, S., McNeill, A., Trilling, D.E., Sickafoose, A.A., Denneau, L., Flewelling, H., Heinze, A., Tonry, J.L., 2020. Investigating taxonomic diversity within asteroid families through {ATLAS} dual-band photometry. Astrophys. J. Suppl. Ser. 247, 13. https://doi.org/10.3847/1538-4365/ab5e88.

Fornasier, S., Lantz, C., Barucci, M., Lazzarin, M., 2014. Aqueous alteration on main belt primitive asteroids: results from visible spectroscopy. Icarus 233, 163–178. https://doi.org/10.1016/j.icarus.2014.01.040.

Fornasier, S., Lantz, C., Perna, D., Campins, H., Barucci, M., Nesvorny, D., 2016. Spectral variability on primitive asteroids of the themis and beagle families: space weathering effects or parent body heterogeneity? Icarus 269, 1–14. https://doi.org/10.1016/j.icarus.2016.01.002.

Gehrels, T., 1956. Photometric studies of asteroids. v. the light-curve and phase function of 20 massalia. Astrophys. J. 123 https://doi.org/10.1086/146166.

Grav, T., Mainzer, A., Spahr, T., Masiero, J., Bauer, J.M., Cutri, R.M., Kramer, E., Sonnett, S., 2019. Neocam survey cadence and simulation. In: Lunar and Planetary Science Conference, p. 3175.

Harris, A.W., Lagerros, J.S.V., 2002. Asteroids in the Thermal Infrared, pp. 205–218.

Hodapp, K.W., Kaiser, N., Aussel, H., Burgett, W., Chambers, K.C., Chun, M., Dombeck, T., Douglas, A., Hafner, D., Heasley, J., Hoblitt, J., Hude, C., Isani, S., Jedicke, R., Jewitt, D., Laux, U., Luppino, G.A., Lupton, R., Maberry, M., Magnier, E., Mannery, E., Monet, D., Morgan, J., Onaka, P., Price, P., Ryan, A., Siegmund, W., Szapudi, I., Tonry, J., Wainscoat, R., Waterson, M., 2004. Design of the pan-starrs telescopes. Astronomische Nachrichten 325, 636–642. https://doi.org/10.1002/asna.200410300.

Huaman, M., Carruba, V., Domingos, R.C., Aljbaae, S., 2017. The asteroid population in g-type non-linear secular resonances. In: Monthly Notices of the Royal Astronomical Society, 468, pp. 4982–4991. https://doi.org/10.1093/mnras/stx843.

Ivezić, V., Lupton, R.H., Jurić, M., Tabachnik, S., Quinn, T., Gunn, J.E., Knapp, G.R., Rockosi, C.M., Brinkmann, J., 2002. Color confirmation of asteroid families. Astron. J. 124, 2943–2948. URL: doi:https://doi.org/10.1086/344077, doi:https://doi.org/10.1086/344077.

Jones, R.L., None, N., Chesley, S.R., Connolly, A.J., Harris, A.W., Ivezic, Z., Knezevic, Z., Kubica, J., Milani, A., Trilling, D.E., 2009. Solar system science with lsst. Earth Moon Planet. 105, 101–105. https://doi.org/10.1007/s11038-009-9305-z.

Kaasalainen, S., Piironen, J., Kaasalainen, M., Harris, A., Muinonen, K., Cellino, A., 2003. Asteroid photometric and polarimet- ric phase curves: empirical interpretation. Icarus 161, 34–46. https://doi.org/10.1016/s0019-1035(02)00020-9.

Karttunen, H., Bowell, E., 1989. Modelling asteroid brightness variations. ii - the uninterpretability of light curves and phase curves. A&A 208, 320–326.

Knezevic, Z., Milani, A., 2000. Celestial Mechanics and Dynamical Astronomy, 78, pp. 17–46. https://doi.org/10.1023/a:1011187405509.

Li, J.Y., Helfenstein, P., Buratti, B., Takir, D., Clark, B., 2015. Asteroid Photometry, pp. 129–150. https://doi.org/10.2458/azu_uapress_9780816532131-ch007.

LSST Science Collaboration, 2009. Lsst Science Book, version 2.0. arXiv e-prints arXiv:0912.0201arXiv:0912.0201.

Marciniak, A., Pilcher, F., Oszkiewicz, D., Santana-Ros, T., Urakawa, S., Fauvaud, S., Kankiewicz, P., Tychoniec, L., Fauvaud, M., Hirsch, R., Horbowicz, J., Kamiński, K., Konstanciak, I., Kosturkiewicz, E., Murawiecka, M., Nadolny, J., Nishiyama, K., Okumura, S., Polińska, M., Richard, F., Sakamoto, T., Sobkowiak, K., Stachowski, G., Trela, P., 2015. Against the biases in spins and shapes of asteroids. Planet. Space Sci. 118, 256–266. https://doi.org/10.1016/j.pss.2015.06.002.

Marsset, M., DeMeo, F.E., Binzel, R.P., Bus, S.J., Burbine, T.H., Burt, B., Moskovitz, N., Polishook, D., Rivkin, A.S., Slivan, S.M., Thomas, C., 2020. Twenty years of spex: accuracy limits of spectral slope measurements in asteroid spectroscopy. The Astrophysical Journal Supplement Series 247 (2), 73–85. https://doi.org/10.3847/1538-4365/ab7b5f.

Masiero, J.R., Mainzer, A.K., Grav, T., Bauer, J.M., Cutri, R.M., Dailey, J., Eisenhardt, P. R.M., McMillan, R.S., Spahr, T.B., Skrutskie, M.F., Tholen, D., Walker, R.G., Wright, E.L., DeBaun, E., Elsbury, D., Gautier, T.I., Gomillion, S., Wilkins, A., 2011. Main belt asteroids with wise/neowise. i. preliminary albedos and diameters. ApJ 741–768. https://doi.org/10.1088/0004-637X/741/2/68 arXiv:1109.4096.

Masiero, J.R., Mainzer, A.K., Bauer, J.M., Grav, T., Nugent, C.R., Stevenson, R., 2013. Asteroid family identification using the hierarchical clustering method andwise/neowise physical properties. Astrophys. J. 770 (7) https://doi.org/10.1088/0004-637x/770/1/7.

Masiero, J.R., Grav, T., Mainzer, A.K., Nugent, C.R., Bauer, J.M., Stevenson, R., Sonnett, S., 2014. Main-belt asteroids with- wise/neowise: near-infrared albedos. Astrophys. J. 791 (121) https://doi.org/10.1088/0004-637x/791/2/121.

Masiero, J.R., Mainzer, A.K., Wright, E.L., 2018. A family-based method of quantifying neowise diameter errors. Astron. J. 156, 62. https://doi.org/10.3847/1538-3881/aacbd4.

Milani, A., Knežević, Z., 1992. Asteroid proper elements and secular resonances. Icarus 98, 211–232. https://doi.org/10.1016/0019-1035(92)90091-k.

Milani, A., Cellino, A., Knežević, Z., Novaković, B., Spoto, F., Paolicchi, P., 2014. Asteroid families classification: exploiting very large datasets. Icarus 239, 46–73. https://doi.org/10.1016/j.icarus.2014.05.039.

Mommert, M., Kelley, M., De Val-Borro, M., Li, J.Y., Guzman, G., Sipőcz, B., Ďurech, J., Granvik, M., Grundy, W., Moskovitz, N., Penttilä, A., Samarasinha, N., 2019. sbpy: a python module for small-body planetary astronomy. J. Open Source Softw. 4, 1426. https://doi.org/10.21105/joss.01426.

Mothné-Diniz, T., Roig, F., Carvano, J., 2005. Reanalysis of asteroid families structure through visible spectroscopy. Icarus 174, 54–80. https://doi.org/10.1016/j.icarus.2004.10.002.

Muinonen, K., Piironen, J., Kaasalainen, S., Cellino, A., 2002. Asteroid photometric and polarimetric phase curves: empirical modeling. Mem. Soc. Astron. Italiana 73, 716.

Muinonen, K., Belskaya, I.N., Cellino, A., Delbò, M., Levasseur-Regourd, A.C., Penttilä, A., Tedesco, E.F., 2010. A three-parameter magnitude phase function for asteroids. Icarus 209, 542–555. URL: https://api.elsevier.com/content/article/PII:S001910351000151X?httpAccept=text/plain. https://doi.org/10.1016/j.icarus.2010.04.003.

Nathues, A., 2010. Spectral study of the eunomia asteroid family part ii: the small bodies. Icarus 208, 252–275. https://doi.org/10.1016/j.icarus.2010.02.011.

Nugent, C.R., Mainzer, A., Masiero, J., Bauer, J., Cutri, R.M., Grav, T., Kramer, E., Sonnett, S., Stevenson, R., Wright, E.L., 2015. Neowise reactivation mission year one: preliminary asteroid diameters and albedos. ApJ 814, 117. https://doi.org/10.1088/0004-637X/814/2/117 arXiv:1509.02522.

Ostro, S.J., Connelly, R., 1984. Convex profiles from asteroid lightcurves. Icarus 57, 443–463. https://doi.org/10.1016/0019-1035(84)90129-5.

Oszkiewicz, D., Muinonen, K., Bowell, E., Trilling, D., Penttilä, A., Pieniluoma, T., Wasserman, L., Enga, M.T., 2011. Online multi-parameter phase-curve fitting and application to a large corpus of asteroid photometric data. J. Quant. Spectrosc. Radiat. Transf. 112, 1919–1929. URL: https://api.elsevier.com/content/article/PII:S0022407311001130?httpAccept=text/plain. https://doi.org/10.1016/j.jqsrt.2011.03.003.

Oszkiewicz, D.A., Bowell, E., Wasserman, L., Muinonen, K., Penttilä, A., Pieniluoma, T., Trilling, D.E., Thomas, C.A., 2012. Asteroid taxonomic signatures from photometric phase curves. Icarus 219, 283–296. URL: https://api.elsevier.com/content/article/PII:S0019103512000760?httpAccept=text/plain. https://doi.org/10.1016/j.icarus.2012.02.028.

Parker, A., Ivezić, V., Jurić, M., Lupton, R., Sekora, M., Kowalski, A., 2008. The size distributions of asteroid families in the sdss moving object catalog 4. Icarus 198, 138–155. https://doi.org/10.1016/j.icarus.2008.07.002.

Peacock, J.A., 1983. Two-dimensional goodness-of-fit testing in astronomy. In: Monthly Notices of the Royal Astronomical Society, 202, pp. 615–627. https://doi.org/10.1093/mnras/202.3.615.

Penttilä, A., Shevchenko, V., Wilkman, O., Muinonen, K., 2016. H, g 1, g 2 photometric phase function extended to low-accuracy data. Planet. Space Sci. 123, 117–125. URL: https://api.elsevier.com/content/article/PII:S0032063315002408?httpAccept=text/plain. https://doi.org/10.1016/j.pss.2015.08.010.

Popescu, M., Licandro, J., Morate, D., de León, J., Nedelcu, D.A., Rebolo, R., McMahon, R.G., Gonzalez-Solares, E., Irwin, M., 2016. Near-infrared colors of minor planets recovered from vista-vhs survey (movis). A&A 591, A115. https://doi.org/10.1051/0004-6361/201628163 arXiv:1605.05594.

Popescu, M., Licandro, J., Carvano, J.M., Stoicescu, R., de León, J., Morate, D., Boacă, I. L., Cristescu, C.P., 2018. Taxonomic classification of asteroids based on movis near-infrared colors. Astron. Astrophys. 617, A12. https://doi.org/10.1051/0004-6361/201833023.

Rivkin, A.S., 2012. The fraction of hydrated c-complex asteroids in the asteroid belt from sdss data. Icarus 221, 744–752. https://doi.org/10.1016/j.icarus.2012.08.042.

Rodrigo, C., Solano, E., Bayo, A., 2012. Svo Filter Profile Service Version 1.0. https://doi.org/10.5479/ads/bib/2012ivoa.rept.1015r.

Salvatier, J., Wiecki, T.V., Fonnesbeck, C., 2016. Probabilistic programming in python using pymc3. PeerJ Comput. Sci. 2, e55. https://doi.org/10.7717/peerj-cs.55.

Sanchez, J.A., Reddy, V., Nathues, A., Cloutis, E.A., Mann, P., Hiesinger, H., 2012. Phase reddening on near-earth asteroids: implications for mineralogical analysis, space weathering and taxonomic classification. Icarus 220, 36–50. https://doi.org/10.1016/j.icarus.2012.04.008 arXiv:1205.0248.

Shevchenko, V., Belskaya, I., Chiorny, V., Piironen, J., Erikson, A., Neukum, G., Mohamed, R., 1997. Asteroid observations at low phase angles. i. 50 Virginia, 91 Aegina and 102 Miriam. Planet. Space Sci. 45, 1615–1623. https://doi.org/10.1016/s0032-0633(97)00131-1.

Shevchenko, V.G., Belskaya, I.N., Krugly, Y.N., Chiomy, V.G., Gaftonyuk, N.M., 2002. Asteroid observations at low phase angles. ii. 5 Astraea, 75 Eurydike, 77 Frigga, 105 Artemis, 119 Althaea, 124 Alkeste, and 201 Penelope. Icarus 155, 365–374. https://doi.org/10.1006/icar.2001.6651.

Shevchenko, V., Chiorny, V., Gaftonyuk, N., Krugly, Y., Belskaya, I., Tereschenko, I., Velichko, F., 2008. Asteroid observations at low phase angles iii. brightness behavior of dark asteroids. Icarus 196, 601–611. https://doi.org/10.1016/j.icarus.2008.03.015.

Shevchenko, V.G., Belskaya, I.N., Muinonen, K., Penttilä, A., Krugly, Y.N., Velichko, F.P., Chiorny, V.G., Slyusarev, I.G., Gaftonyuk, N.M., Tereschenko, I.A., 2016. Asteroid observations at low phase angles. iv. average parameters for the new h, g 1, g 2 magnitude system. Planet. Space Sci. 123, 101–116. URL: https://api.elsevier.com/content/article/PII:S0032063315003566?httpAccept=text/plain. https://doi.org/10.1016/j.pss.2015.11.007.

Shkuratov, Y., Ovcharenko, A., Zubko, E., Miloslavskaya, O., Muinonen, K., Piironen, J., Nelson, R., Smythe, W., Rosenbush, V., Helfenstein, P., 2002. The opposition effect and negative polarization of structural analogs for planetary regoliths. Icarus 159, 396–416. https://doi.org/10.1006/icar.2002.6923.

Spoto, F., Milani, A., Knežević, Z., 2015. Asteroid family ages. Icarus 257, 275–289. https://doi.org/10.1016/j.icarus.2015.04.041.

Surdej, A., Surdej, J., 1978. Asteroid lightcurves simulated by the rotation of a three-axes ellipsoid model. A&A 66, 31–36.

Szabó, G.M., Ivezić, V., Jurić, M., Lupton, R., Kiss, L.L., 2004. Colour variability of asteroids in the sloan digital sky survey moving object catalog. In: Monthly Notices of the Royal Astronomical Society, 348, pp. 987–998. https://doi.org/10.1111/j.1365-2966.2004.07426.x.

Tedesco, E.F., Williams, J.G., Matson, D.L., Weeder, G.J., Gradie, J.C., Lebofsky, L.A., 1989. A three-parameter asteroid taxonomy. Astron. J. 97, 580. https://doi.org/10.1086/115007.

Tholen, D.J., 1984. Asteroid Taxonomy from Cluster Analysis of Photometry. phdthesis, University of Arizona, Tucson.

Tonry, J.L., 2011. An early warning system for asteroid impact. Publ. Astron. Soc. Pac. 123, 58–73. https://doi.org/10.1086/657997.

Tonry, J.L., Denneau, L., Heinze, A.N., Stalder, B., Smith, K.W., Smartt, S.J., Stubbs, C. W., Weiland, H.J., Rest, A., 2018. Atlas: a high-cadence all-sky survey system. Publ. Astron. Soc. Pac. 130 https://doi.org/10.1088/1538-3873/aabadf. URL: http://stacks.iop.org/1538-3873/130/i=988/a=064505?key=crossref.e571d7afee1776599bad86be6fcc932e.

Vereš, P., Jedicke, R., Fitzsimmons, A., Denneau, L., Granvik, M., Bolin, B., Chastel, S., Wainscoat, R.J., Burgett, W.S., Chambers, K.C., Flewelling, H., Kaiser, N., Magnier, E.A., Morgan, J.S., Price, P.A., Tonry, J.L., Waters, C., 2015. Absolute magnitudes and slope parameters for 250,000 asteroids observed by pan-starrs ps1 – preliminary results. Icarus 261, 34–47. https://doi.org/10.1016/j.icarus.2015.08.007.

Viikinkoski, M., Hanuš, J., Kaasalainen, M., Marchis, F., Ďurech, J., 2017. Adaptive optics and lightcurve data of asteroids: twenty shape models and information content analysis. Astron. Astrophys. 607, A117. https://doi.org/10.1051/0004-6361/201731456.

Warner, B.D., Harris, A.W., Pravec, P., 2009. The asteroid lightcurve database. Icarus 202, 134–146. https://doi.org/10.1016/j.icarus.2009.02.003.

Zappalà, V., Cellino, A., Farinella, P., Knezevic, Z., 1990. Asteroid families. I - identification by hierarchical clustering and reliability assessment. Astron. J. 100, 2030. https://doi.org/10.1086/115658.

Zappalà, V., Cellino, A., Di Martino, M., Migliorini, F., Paolicchi, P., 1997. Maria's family: physical structure and possible implications for the origin of giant neas. Icarus 129, 1–20. https://doi.org/10.1006/icar.1997.5749.